A Wide-Field Multi-band Dark Energy Camera (DECam) and Gaia DR2 Study of the outskirts of ωCentauri

Kathleen Grabowski

Brian Yanny

and

DES collaborators

ABSTRACT

We match wide-field (1 degree) multi-band ($ugrizY$) positions of stars in the field of the large globular cluster ωCentauri obtained with DECam to the Gaia DR2 catalog with proper motions and parallax. A joint table is presented and used to explore changing stellar populations with radius from the center and to search for the existence of near-field extra-tidal cluster members. With this joint catalog we find evidence that multiple sub-giant and giant branches are still present at distances of $40' - 55'$ from the cluster center and in fact the most metal rich giant branch population is less centrally concentrated than other stellar populations. Our cataloged table is highly complete in the DES filters at radii of $2'$ to $50'$ from the center of the cluster for objects with magnitudes $11 < r < 22.5$. Gaia allows us to study members at radii from $10'$ to $180'$ to magnitude $G \sim 20.5$. We present evidence of significant but small numbers of extra-tidal members of the cluster at radii $72' < r < 84'$, at position angles of $\sim 105°$. Closer in, there is an asymmetric distribution of outer cluster stars, favoring P.A.s $\sim 150° - 270°$. We discuss the origin of these preferred azimuths, and suggest that both the intrinsic rotation of ωCentauri and tidal interactions due to past close passages near the Galactic Center are responsible for the extra-tidal and near tidal asymmetric distribution of stars. There is no evidence for asymmetric extra-tidal star distributions at radii $84' < r < 180'$. We note a discrepancy in the center position of the cluster as reported by Gaia DR2 compared with earlier studies and suggest it is a result of Gaia DR2 incompleteness in the central regions.

Subject headings: globular clusters: general, globular clusters: individual (NGC 5139), techniques:photometry, astrometry

1. Introduction

1.1. The Dark Energy Survey

The Dark Energy Survey (DES) has a primary mission to study and constrain the equation of state for an apparent dark energy component to the contents of the universe (Frieman et al. 2005). The techniques include analyzing baryonic acoustic oscillations, supernovae, strong and weak gravitational lensing, and galaxy clusters. DES aims to reduce the uncertainty on w to the few percent level and constrain its time derivative (Frieman et al. 2013). These techniques rely on accurate multi-color astrometry, photometry as well as shape measurements of more than one hundred million of faint ($i \sim 24$) galaxies. Stellar measurements, in turn, anchor DES's calibration effort, where accurately characterizing the point spread function (PSF) for each field observed from stellar sources reduces systematic errors on the shapes of the extended sources. Additionally, the photometric and astrometric calibration of DECam exposures, both relative and absolute, are essential to meeting the DES science goals. We report here an analysis of stars in early DECam exposures obtained of the ωCen globular cluster and surrounding field, combined with recently released Gaia DR2 proper motion catalogs of the same region of sky.

2. Omega Centauri

There are approximately 150 globular clusters known around the Milky Way (Harris 2010). ωCen is the largest known cluster and shares many properties with the cores of dwarf galaxies (Bekki & Freeman 2003).

ωCen (NGC 5139) is centered on (RA, DEC)=(201.6968, -47.4795). The corresponding Galactic coordinates (l,b)= (309.10, 14.97) place the cluster slightly above the plane of the disk (Z=+1.3 kpc). Its heliocentric distance is 5.2 kiloparsecs (kpc) and it is 6.4 kpc from the Galactic Center. Its core radius is 2.35′, the half-light radius is 5′, and the concentration is 1.24. The classic value for the cluster's tidal radius is 48′ from Harris (2010), however Marconi et al. (2014) find a significantly larger value of 72′ (see below). At least the central parts of the cluster's stars are rotating on an axis at position angle 10° E of N, inclined at approximately 40° (Bianchini et al. 2018).

This cluster has been studied extensively in the literature, including searches for stars originating from the cluster, now present in the near and far surrounding field.

2.0.1. Near field ωCen Tidal Tail Searches

Leon et al. (2000) found possible evidence for tidal tails of ωCen perpendicular to the Galactic Center, which could indicate the effect of shocking on passage through the Galactic disk. Law et al. (2003), however, showed that accounting for differential reddening argues against the presence of these tidal tails. Law et al. (2003) compared the linear surface density contours for raw Two-Micron All Sky Survey (2MASS) data to the contours for data dereddened by the dust maps of Schlegel et al. (1998). They find that the non-dereddened contours are similar to Figure 14a in Leon et al. (2000) and that the dereddened contours show no evidence for a tidal tail. Da Costa & Coleman (2008) looked for cluster members beyond the tidal radius and found that of 28 stars selected to have heliocentric velocities within the range of the cluster, six also have a proper motion and line-strength parameters consistent with the cluster. Based on the spectroscopy of these six stars within 3 degrees of the cluster, there is no evidence for a significant extra-tidal population close (within a few degrees) to the cluster beyond its tidal radius. More recently, Fernández-Trincado et al. (2014) imaged areas nearly 6 degrees from the center of the cluster, finding 37 new RR Lyrae beyond the tidal radius. Further analysis of a sub-sample of stars that were within 3.5-9 kpc from the sun do not have consistent periods with the cluster RRLyrae stars, and stars that are beyond the tidal radius have radial velocities consistent with the halo or thick disk. Still more recently, Marconi et al. (2014) re-examined stellar density contour again and found some low-significance evidence for excess stars 1 to 2 degrees away from the cluster core.

2.0.2. Far field extra-tidal star searches

While near-field searches for extra-tidal stars have had limited success, the retrograde orbit of the cluster allows for kinematic information to be used to search further afield. It is possible that there may be stars from ωCen scattered about the galaxy due to an earlier epoch of tidal stripping, during the last time the cluster passed close to the Galactic center. Majewski et al. (2012) finds 35 stars from the Grid Giant Star Survey in the solar neighborhood that have barium abundances and retrograde motions consistent with membership to the cluster. Based on the overall low number of retrograde stars within the area, metallicity signatures of the candidate cluster stars lead them to conclude that ωCen is a main source of retrograde stars within the solar neighborhood. Most recently, Myeong et al. (2018) combined Gaia DR1 kinematics with SDSS photometry and located several star groups kiloparsecs away from the cluster's current position, but consistent with its past orbital history.

Below we largely confirm the absence of significant tidal tail stars within about 1 degree of the cluster using DECam images. Using Gaia DR2 proper motions, we do find a small number (~ 9) of near-field extra-tidal stars beyond the tidal radius of 72 arcminutes, at a preferred position angle (PA $=105°$) around the cluster. but no significant asymmetrically-placed detections beyond 84 arcminutes from cluster center. Closer in, there is a 3σ excess of about 77 cluster members at radii between $36'$ and $60'$ at P.A. between $150°$ and $270°$.

2.0.3. Multiple stellar populations in ωCen

There are several large clusters, including M54 near the center of the dwarf galaxy Sagittarius, that have multiple populations of stars with a range of metallicities. In ωCen, these are most noticeable as separate sub-giant branches in the color-magnitude diagrams obtained with blue or ultraviolet filters. For instance, Bellini et al. (2010) found six distinct populations are apparent within $15'$ of the cluster center.

The cluster also has at least 2 main sequences visible. Remarkably, Piotto et al. (2005) found that the bluer branch of the main sequence in ωCen is more metal-rich and less populous than the red branch, although the two populations have the same radial velocity. They postulate that the cluster is massive enough to retain supernovae of 10 to 14 solar masses, while the ejecta of higher-mass supernovae escapes. The color-metallicity anomaly may be related to unusual Helium abundance (Bellini et al. 2009). Extensive studies have been made of the unusual abundance patterns of ωCen giants (i.e. Calamida et al. (2009)). Lee et al. (2009) suggested that a massive dwarf galaxy would be large enough to retain supernovae winds and remain metal-enriched, although the present size of the remaining globular cluster is too small. It is also found that the metal-rich red giant branch (RGB) is 2 Gyr younger than the metal-poor RGB, which may imply instead two merging dwarf galaxies or that a progressively less massive cluster would be less likely to retain metal-rich gas after a supernova explosion.

We will show below that the multiple sub-giant branches in ωCen extend well beyond just the central core regions previously studied and we compare the proper motions of stars from different sections of the color-magnitude diagram.

2.0.4. Blue Hook population in ωCen

Another feature peculiar to ωCen and only a few other massive clusters (i.e. NGC 2808) are very extended horizontal branches, with distinctive blue hook features and gaps in the horizontal branch population(s) when displayed in color magnitude diagrams. See Whitney et al. (1998); D'Cruz et al. (2000), for discussion of the mechanism that causes the clump at the faint, blue end of the horizontal branch at magnitude 18 and u-g $\sim$ 0. Bailyn et al. (1992) found that between $3'$ -$14'$ from the center of the ωCen, a blue subdwarf population was bluer and fainter than the classical HB stars. This may be due to having a helium core, but a thin hydrogen envelope unable to support shell burning. Brown et al. (2001) suggested that the mechanism for the extended horizontal branch properties is that a helium flash occurs when a star is on the white dwarf cooling curve, and the convection causes mixing between the layers.

We show below that distribution of blue hook stars in ωCen extends throughout the cluster, at least 1/2 way to the tidal radius. That is, this population is not confined only to the cluster's most central regions.

3. Observations and Processing

3.1. DECam and the DES Science Verification period

DES observations were obtained with the 4-meter Blanco telescope at the Cerro Tololo Inter-American Observatory (CTIO) using the DECam 62-CCD mosaic camera (Flaugher et al. 2015). Images were taken in $u,g,r,i,z,$ and Y photometric filters with wavelengths ranging from 350-1000 nm. The field of view of DECam has a radius of approximately 1 degree and the exposures reach a depth of $i \sim 22.5$ (3 sigma) in 60 seconds. First light was in September 2012, and DECam exposures obtained through February 2013 were part of a DES and DECam science verification data set with the purpose of understanding and correcting issues with the instrument system as well as obtaining initial instrument characterization and calibration. All raw exposures from the science verification period are publicly available as part of the NOAO Science Archive (http://archive.noao.edu).

Sets of four dithered (offsets of $\sim 8'$) exposures, centered on the cluster, were all obtained the night of 2013 Feb 21 for 3 and 30 seconds in the $g,r,i,z,$ and Y filters, as well as 6 and 60 seconds in the u filter for a total of 8 exposures in each of six filters. The shorter exposure times in each band allow stars 3 to 5 magnitudes brighter than the DES survey's saturation limit (mag ~ 15.5 for 90s) to be explored. Table 1 lists the DECam exposures used in this analysis.

3.2. DAOPHOT and SExtractor

The quality of positions and magnitudes for measured star images is dependent on the accuracy of the photometric processing, and in particular, on proper characterization of the point spread function (PSF). The DES uses processing software based on the SExtractor set of related packages (E. Bertin, http://astromatic.net). SExtractor does characterize the PSF in its photometry (PSFEx), however since DES primarily is a galaxy survey, the standard DES processing is not optimized for crowded fields consisting of nearly all stellar objects. The package DAOPHOT, on the other hand, uses an PSF-fitting algorithm which was designed for use in crowded star fields such as globular clusters (Stetson 1987). DAOPHOT allows us to resolve overlapping stellar images with high completeness to within about $5'$ from the cluster center, and with decreasing completeness to within about $2'$ from the center (see Figure 4 below). With the galaxy-and-star modeling package SExtractor, in its default configuration, full completeness is limited to regions greater than $\sim 10'$ from the center. In what follows we use DAOPHOT for the PSF fitting and object measurement of stars, and the astromatic.net software package SCAMP to solve for the geometric camera solution and for the combined astrometry of all ωCen exposures jointly.

Band	Time (seconds)	Exposure Number	RA	Dec.
u	60	180787	201.69700000	-47.47947200
		180788	201.73866700	-47.47947200
		180789	201.73866700	-47.43780600
		180790	201.69700000	-47.43780600
	6	180791	201.69700000	-47.47947200
		180792	201.73866700	-47.47947200
		180793	201.73866700	-47.43780600
		180794	201.69700000	-47.43780600
g	30	180795	201.69700000	-47.47947200
		180796	201.73866700	-47.47947200
		180797	201.73866700	-47.43780600
		180798	201.69700000	-47.43780600
	3	180799	201.69700000	-47.47947200
		180800	201.73866700	-47.47947200
		180801	201.73866700	-47.43780600
		180802	201.69700000	-47.43780600
r	30	180803	201.69700000	-47.47947200
		180804	201.73866700	-47.47947200
		180805	201.73866700	-47.43780600
		180806	201.69700000	-47.43780600
	3	180807	201.69700000	-47.47947200
		180808	201.73866700	-47.47947200
		180809	201.73866700	-47.43780600
		180810	201.69700000	-47.43780600
i	30	180811	201.69700000	-47.47947200
		180812	201.73866700	-47.47947200
		180813	201.73866700	-47.43780600
		180814	201.69700000	-47.43780600
	3	180815	201.69700000	-47.47947200
		180816	201.73866700	-47.47947200
		180817	201.73866700	-47.43780600
		180818	201.69700000	-47.43780600
z	30	180819	201.69700000	-47.47947200
		180820	201.73866700	-47.47947200
		180821	201.73866700	-47.43780600
		180822	201.69700000	-47.43780600
	3	180823	201.69700000	-47.47947200
		180824	201.73866700	-47.47947200
		180825	201.73866700	-47.43780600
		180826	201.69700000	-47.43780600
Y	30	180827	201.69700000	-47.47947200
		180828	201.73866700	-47.47947200
		180829	201.73866700	-47.43780600
		180830	201.69700000	-47.43780600
	3	180831	201.69700000	-47.47947200
		180832	201.73866700	-47.47947200
		180833	201.73866700	-47.43780600
		180834	201.69700000	-47.43780600

Table 1: Exposure Table

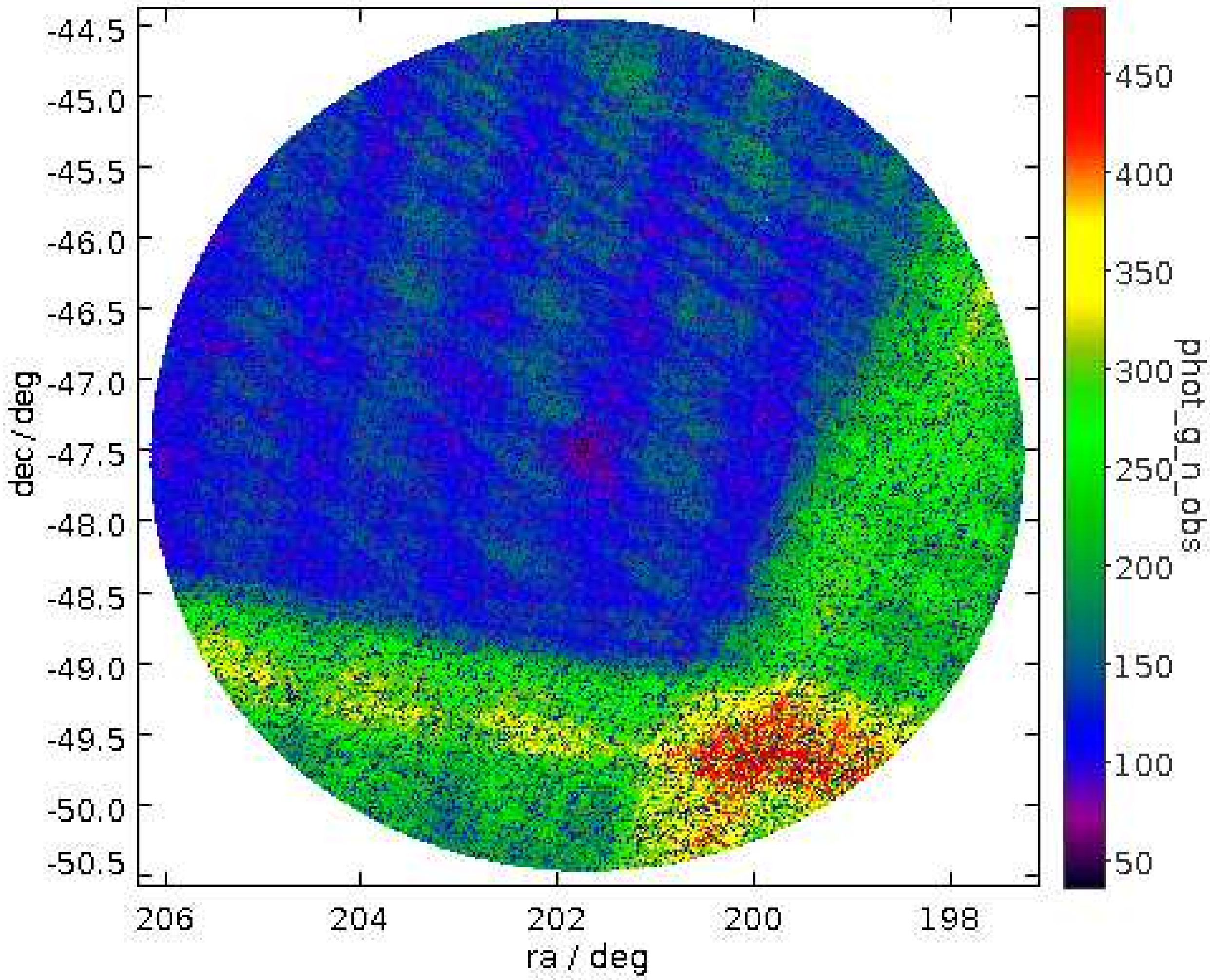

Fig. 1.— The completeness varies in the area 3 degrees around the cluster, based on the number of observations in the G band. Note the limited number of observations in the very center of the cluster field.

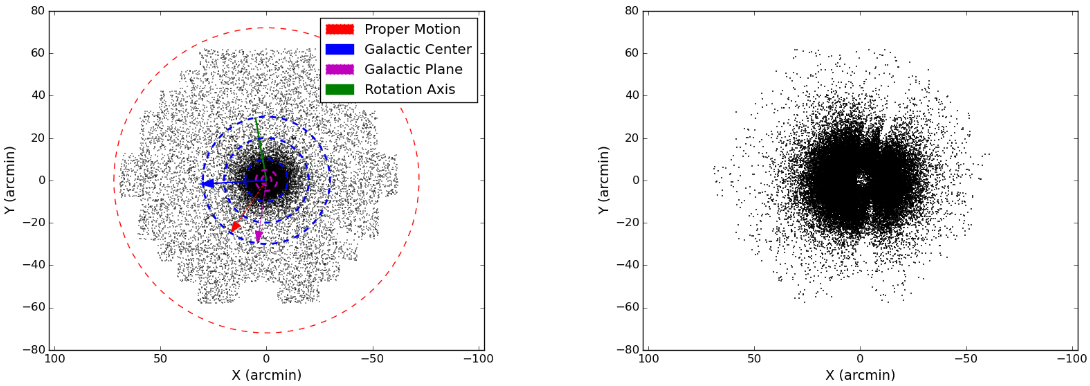

Fig. 2.— The positions of giant branch stars with DES photometry g_0 <17.2. There is no information from a DECam CCD near the bottom of the figure. The magenta rings in the center are at the core radius of 2.37′ and the half-light radius at 5′. The DECam-only catalog of cluster stars is highly complete towards the center. Radii of 10′, 20′, and 30′ are shown in dashed blue lines, and the tidal radius at 72′ is shown in a red dashed line. The proper motion (corrected for solar reflex motion) of the the cluster is indicated with a red dashed arrow and the rotation axis of the cluster is shown with a green line. The direction towards the Galactic Center is indicated with a solid blue line, while the direction towards the Galactic Plane is shown in magenta. The right panel shows the incompleteness of proper-motion selected cluster stars from Gaia.

3.3. Processing steps

DECam exposures consist of 61 separate CCD images (one CCD in the DECam's mosaic was not functioning at the time of the observations), which are initially processed using the standard DESDM software routines for detrending the images (Gruendl et al. 2015, in prep., see http://data.darkenergysurvey.org/aux/releasenotes /DESDMrelease.html). The scale of DECam is $\sim 0.263''$ pixel^{-1}, smoothly varying with a change in scale of no more than 0.5% from center to edge. The astrometric package SCAMP (E. Bertin, http://astromatic.net) was used to determine an initial astrometric solution for the position of each CCD in each exposure on the sky, good to about 150 mas relative to an external catalog such as UCAC-4 (Zacharias et al. 2013). A second round of SCAMP processing was then done, solving simultaneously for the best relative positions of the four 30s i and four 30s r band exposures as these were determined to have the best astrometry. These relative positions are good to about 15 mas for each star of brightness $i < 18$. An explanation of the limitations in positional accuracy is discussed in more detail below.

Now using these registered, detrended images, further processing used the implementation of DAOPHOT available within IRAF. We used the routine 'daofind' to detect all objects at least 1σ above the background to select as many faint sources as possible. Noise sources are removed later when we require a sources to be detected multiple times in multiple filters (within $0.5''$) to be considered a non-spurious detection.

Next, we select a subset of 20-100 high signal-to-noise, isolated stellar objects in each of the DECam's 61 functioning 2k x 4k CCDs to serve as PSF templates. Each chip of each exposure in each filter had its own linearly varying PSF independently determined.

The DECam CCDs, being deep-well CCDs, suffer from an artifact known as the 'brighter-fatter' relation, where the FWHM of the PSF increases significantly for objects brighter than a certain threshold (Plazas et al. 2014). While this effect can and will be corrected in later DES processing releases, for now, we avoid combining fainter (unaffected) and brighter (brighter-fatter afflicted) stars when constructing a PSF for each CCD image simply by excluding the brighter stars from our candidate PSF star lists. To do this we select PSF candidate stars using 'pselect' in DAOPHOT/IRAF, scaling the range appropriately for exposure time and filter sensitivity. A magnitude range of 14 to 18 was adopted for most filters, although the u-band allowed a fainter range of PSF candidates. As the PSF stars are chosen by decreasing brightness and weighted by magnitude, it is likely that the PSF image is dominated by the brighter objects in most cases.

The DAOPHOT parameters for choosing PSF stars were as follows: $-0.5 <$SHARP< 0.8, $|$SROUND$| < 0.1$ and $|$GROUND$| <0.2$. If there were no PSF stars within these magnitude, roundness, and sharpness ranges, we increased the parameters by 0.1 and iterate until we collect at least 20 good quality stars.

The DAOPHOT fit radius parameter was chosen to be 4.5 pixels, approximately the FWHM of the brighter stars, which accounted for some of the variation in width depending on the brightness of the star. We constructed a PSF model of size 30 pixels so that it would be able to subtract the extended wings of brighter cluster stars.

When selecting PSF stars, however, we temporarily adjusted the ‘psfrad’ parameter to choose primarily isolated, uncrowded stars. The DAOPHOT software was able to find a suitable PSF in most cases without further manual intervention. In some cases, however, these measures still were not enough to obtain a good PSF in several of the centrally located DECam CCDs, over which the center of ωCen fell in four dithered exposures per filter and exposure time. For CCDs close to the center of the cluster which contained mostly crowded stars (21,22,27,28,34,35,41,42,47,and 48; for a map of the locations of these CCDs within the DECam focal plane, please see Figure 7 in: http://data.darkenergysurvey.org/aux/releasenotes/
DESDMrelease.html), we avoided selecting PSF stars from a circle that had a radius ranging from 1000-2000 pixels centered on the cluster. These PSF template-star exclusion circles varied from CCD to CCD, filter to filter, and between the 3 and 30-second exposures. The crowding was more noticeable for the longer exposures., requiring larger exclusion areas.

We refer the reader to Morganson et al. (2018) for details of the standard DES data reduction procedure.

3.4. Calculating Average Positions

Pixel (x,y) positions obtained using standard DAOPHOT fitted PSF centroids were converted to on sky (RA,DEC) coordinates using the SCAMP solution as described above.

To measure the most accurate positions, 4 30-second r and 2 30-second i band exposures were matched to each other in each filter, and we used the weighted average equation shown below for 2-8 objects where w=((err)^2+(0.01)^2)$^{-1}$ and m corresponds to the individual magnitudes for a star on each exposure.

$$\bar{m} = \frac{\sum_i w_i \cdot m_i}{\sum_i w_i}$$

$$\sigma_m = \sqrt{\frac{\sum_i (m_i - \bar{m})^2}{\sum_i w_i - \frac{\sum_i w_i^2}{\sum_i w_i}}}$$

A residual plot is available as a SCAMP CHECKPLOT (ASTR_XERROR2D,ASTR_YERROR2D) which demonstrates the accuracy of the positions. This plot was generated for the combined SCAMP solution of all 8 of the 30 second r and i exposures. Inverting the WCS solution (kept to cubic order in x,y) and converting the equatorial coordinate of each averaged star's position back

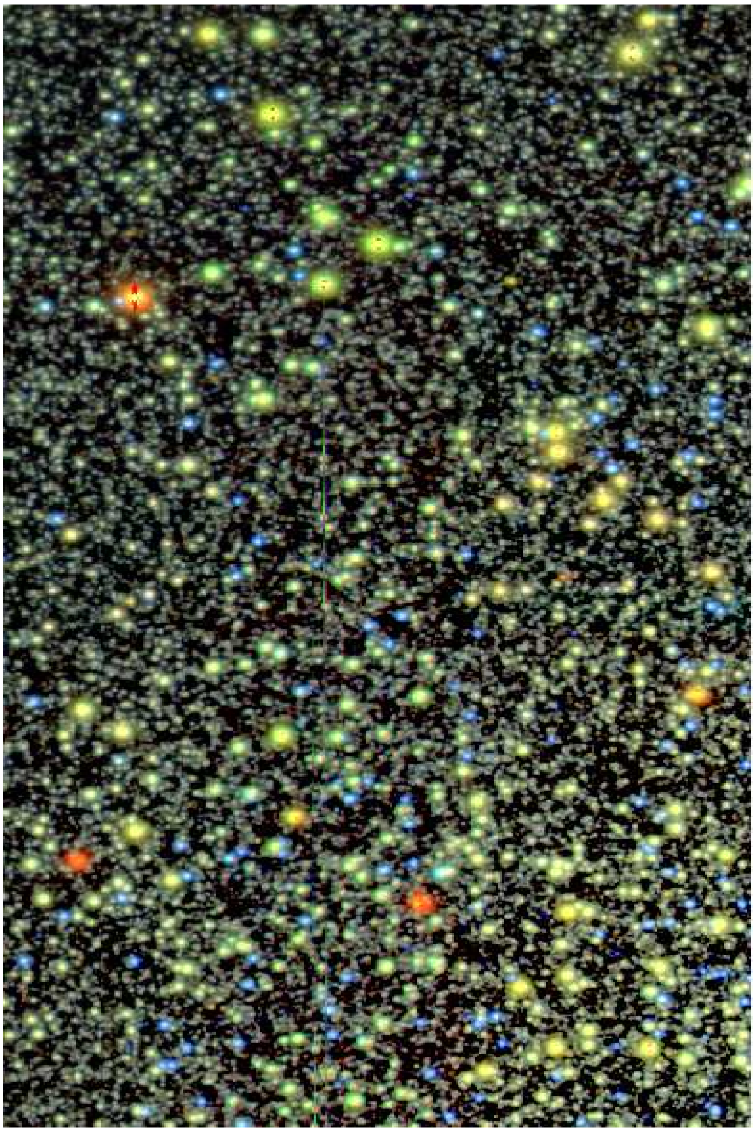

Fig. 3.— RGB image of northwest quadrant of ωCen, from the DES i,g,r bands.

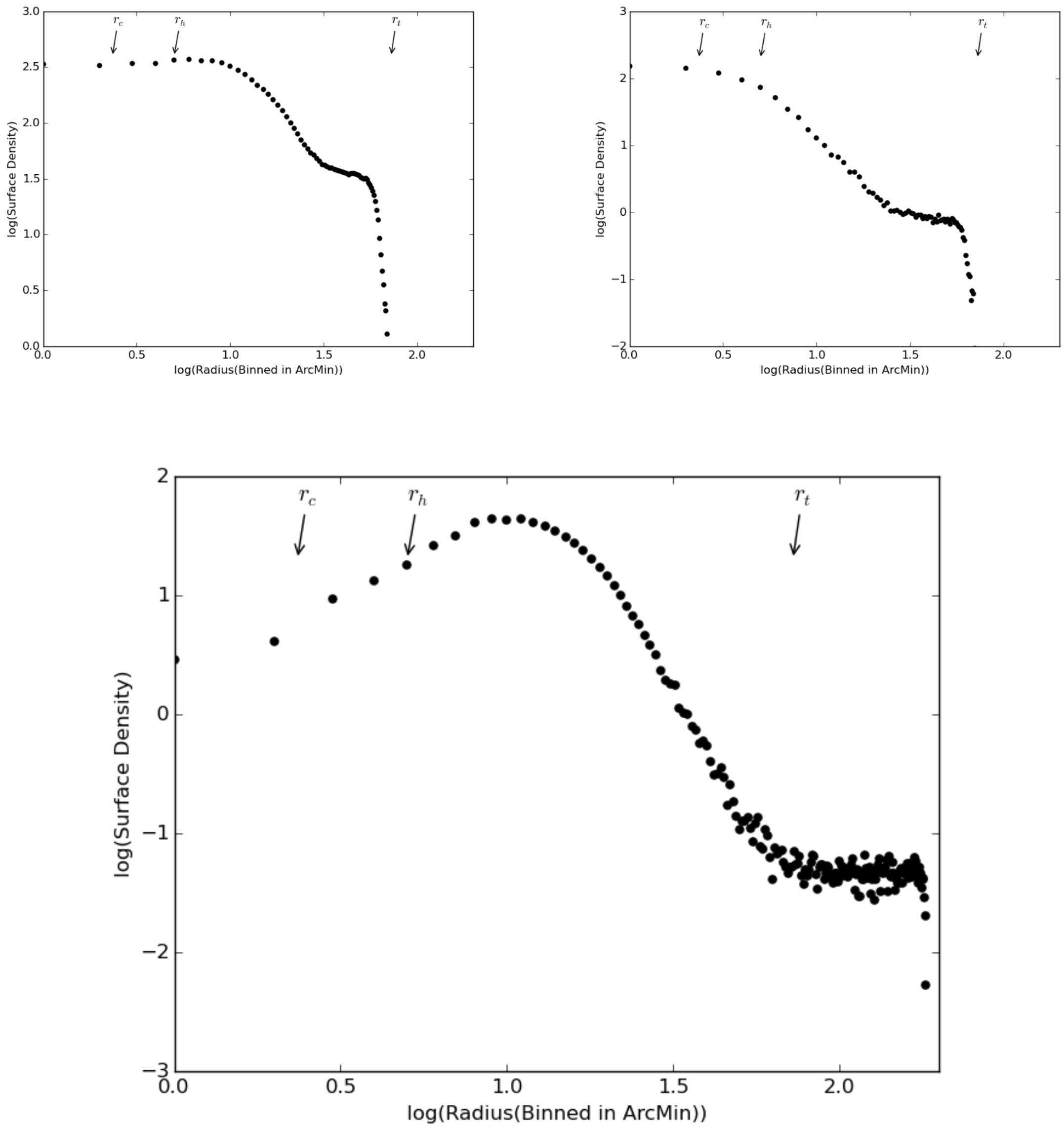

Fig. 4.— Logarithmic surface density of proper motion-selected stars in ωCen as a function of logarithmic radius in arcminutes. The limiting radius of DECam images is 63'.The core radius (r_c=2.37 $'$), the half-light radius (r_h=5 $'$), and the tidal radius (r_t=72$'$) are labeled. The top left panel uses the entire DES catalog (with possible field star contamination) , while the top right panel uses only giant branch stars with g_0 <17.2. The bottom panel shows proper motion-selected stars from Gaia out to 3 degrees from the center of the cluster. Note the incompleteness of the Gaia DR2 subsample chosen at $r < 10'$.

to where the star falls in (X,Y) on each CCD of each exposure, one can compare this (X,Y) with the DAOPHOT centroid (X,Y) position for each object. The residual position errors appear to be circularly symmetric, like tree rings.

Plazas et al. (2014) found that spurious electric fields within the deep CCD wells in individual CCDs modify the effective pixel area. This change affects the photon and electron counts, and is visible in the dome flats. There is a wavelength dependence, appearing with a larger amplitudes (up to 1%) in bluer filters. This can affect the positions that we measure by 13 to 26 mas. Without removing this effect, this is the lower limit on the errors we can get for individual star position measurements.

The effect is repeatable and removable in principle. Future reductions of the DECam exposures for DES and other projects will remove these tree-rings as part of the standard detrending data reduction procedure.

Our present DECam exposures of ωCen have position errors, as measured by comparing overlapping exposures of the same stars with SCAMP, of around 20-40 mas. The error is brightness dependent, with brighter objects ($i < 18$) having the smaller errors (E. Bertin, private communication). It should be possible to improve astrometric accuracy to ~ 5 mas or less if one removes the tree ring effect.

Of course, Gaia DR2 positions are much better where they match DES detections, and one can use Gaia DR2 to improve the overall DECam astrometry.

4. Magnitude Calibration

The amplitude of the DAOPHOT fitted PSF provides the relative magnitude scaling for each object. We go further and place the magnitudes on the DES photometric system using the same techniques that DES itself will use (Tucker et al., in prep). In brief, this calibration system takes place in three stages. First: Since our PSFs are measured independently for each CCD and some PSFs are affected by crowding, we measure the magnitude offsets for the same stars observed multiple times in the 8 dithered exposures in each filter and compute an average offset (in a least-squares sense) for each CCD to place all the CCDs on the same system (within a percent or two). Second: A set of standard star fields on the celestial equator with stars of known, calibrated DES magnitudes (Tucker et al., in prep.) were observed on the same night as ωCen was observed. As long as the night is photometric (it was to within a few percent), and the instrument gain is stable, the relative airmasses and exposure times of the two observations can be used to obtain zeropoints for each ωCene exposure relative to the average of the standard star field exposures. These zeropoints are applied to all stars observed.The final step in the photometric calibration is to place all the magnitudes on the DES system as described in Burke et al. (2018) and applied to released DES data as part of DR1 Abbott et al. (2018). We do this by: processing several of the same expnums listed above through the standard DES processing system described in Morganson et al. (2018) including DES calibration; matching stars and deriving a single offset for each filter $ugrizY$ based on a mean difference for stars of intermediate magnitudes ($\sim 18 - 20$); and applying that offset to the DECam magnitudes here.

The appearance of intensity-dependent of the full-width at half-maximum (FWHM) of the PSF, also known as a brighter-fatter effect, is due to similar electric field effects that cause the tree-ring effect in the flat-field. Antilogus et al. (2014) found that the overfilled pixels become smaller than neighbors, such that brighter stars had a larger FWHM than fainter stars. Over the dynamical range, the linear size of the PSF increases linearly with flux by up to 2%. This effect changes the measured PSF magnitudes of bright stars systematically, and stars with $i < 12$ (and similarly in other bands) in our table will have magnitude errors up to 4%. Future enhancements to the DESDM processing software system will correct for this effect (D. Gruen, in prep.) Using a weighted average to calculate accurate magnitudes, we can decrease the error in color, even as the magnitude errors increase as magnitudes become fainter. From there we can use areas of the color-magnitude diagram to trace different populations around the cluster.

With an astrometric solution in hand, one may construct a multi-color image of the DECam exposures. Figure 3 shows a $5'$ closeup of a region of the northwest quadrant of ωCen. The red, green, and blue colors are driven by the i, g, and r filters respectively. Red giants, Blue Horizontal Branch and main sequence (grey) stars can all be clearly seen.

After calibrating and combining the detected objects (see below) we are able to construct color-magnitude diagrams in various DECam filter combinations. We select stars with colors and magnitudes matching the red giant branch of ωCen in order to explore the coverage completeness of our dithered, combined object catalog:

Figure 4 shows the surface density of proper motion-selected cluster stars as a function of distance from the center in arcminutes. Important distances from the center given by Harris (2010) include the core radius at $2.37'$, half-light radius at $5'$, and tidal radius at $72'$, from Marconi et al. (2014), each labeled in the figure. The top left panel includes all 686,488 stars in the full DES catalog we present here, highly complete towards the center of the cluster, but the data doesn't quite reach the more distant tidal radius of $72'$. The steep decline in the number counts at nearly 1.8 or $63'$ is due to the limiting radius of the field of view of DECam around the cluster. The top right panel traces the proper motion and color-selected red giants shown in Figure 2. The bottom panel includes proper motion selected Gaia stars out to $180'$. While the Gaia data extends to easily show the steep cutoff in cluster members at the tidal radius, at radii less than $r \sim 10'$, the Gaia data are quite incomplete, as shown by the droop in the radial profile in the inner parts where a flat distribution is expected.

4.1. Gaia DR2 catalog

To complement the deep DECam multi-band observations, we query the Gaia DR2 archive interface (Gaia 2018) and select positions, proper motions, parallax, G, bp-rp photometry, radial velocity and associated errors for stars within 3 degrees of the cluster center. We note that while Gaia DR2 is very complete to $G < 17$ for position, proper motion, parallax and G,bp-rp information, between $17.5 < G < 20$ there are patches of incompleteness in coverage. Figure 1 shows the areas of incomplete coverage around the cluster, by color-coding areas by the number of observations in the G magnitude. Striping is visible, and the area southeast of the cluster has nearly 10 times more observations than the area near the center of the cluster.

4.1.1. Proper Motions

The most recent values of proper motion of the cluster are given by Anderson & van der Marel (2009) from HST observations and updated by Gaia DR2 (Helmi et al. 2018) to a value of $(\mu_\alpha, \mu_\delta) = (-3.1925 \pm 0.0022, -6.7445 \pm 0.0019)\text{mas yr}^{-1}$. The space velocity of ωCen may be obtained from the position, proper motion and radial velocity of the cluster and correcting for the solar reflex motion. We find a solar-reflex-corrected proper motion for ωCen of $\mu_{alpha}, \mu_{delta}) = (2.59, -3.85)$ mas/yr assuming 5.16 kpc to the cluster and the solar motion of Dehnen & Binney (1998) and the equations of, for instance, Johnson & Soderblom (1987). Gaia DR2, with proper motion accuracy to about $0.35\,\text{mas yr}^{-1}$ per component for stars in the direction of ωCen, has revolutionized a vast array of studies of stars in and around the Milky Way. We match our DES positions to Gaia DR2 for stars with $G < 20.5$, and use the Gaia proper motions to determine which stars are likely cluster members, even in the outskirts of the cluster, and beyond the tidal radius of about $72'$. By only including likely members of the cluster, the color-magnitude and related diagrams are much cleaner in the outskirts of the cluster and evolution or changing distributions of populations with distance from the cluster center can be more reliably determined.

4.2. Matching DECam and Gaia DR2 catalogs

We match Gaia and DECam catalogs on position with a 1 arcsec matching radius, yielding about 46,300 stars at radii between 1 and 50 arcmin from the cluster center. We further restrict the catalog to keep only objects consistent with the proper motion of the cluster. We use the proper motions reported by Helmi et al. (2018) of (μ_α, μ_δ)=(-3.19,-6.74) mas/yr. We select stars that differ from these proper motion values in each direction by less than 1 mas yr^{-1} with errors less than 1.5 mas yr^{-1}. When selecting stars that have proper motions consistent with the cluster, the completeness for different position angles around the cluster varies with angle. This is noticeable in the left panel of Figure 2, where wedges of the footprint are missing. Though all of the DES and Gaia matches shown here have proper motions consistent with the cluster, based on other criteria they may not be candidate cluster stars. For comparison, in the right panel of Figure 2 we plot red giant branch stars with g_0 <17.2 from the DES catalog alone, which is highly complete in the center. Dithering the exposures fills in the gaps between the CCDs. The magenta rings in the center are at the core radius of $2.37'$ and the half-light radius at $5'$. Radii of $10'$, $20'$, and $30'$ are shown in dashed blue lines, and the tidal radius at $72'$ is shown in a red dashed line. The solar reflex corrected proper motion of the the cluster is indicated with a red dashed arrow and the rotation axis of the cluster is shown with a green line. The direction towards the Galactic Center is indicated with a solid blue line, while the direction towards the Galactic Plane is shown in magenta.

5. Putting it all together: The Catalogs

Where available, a combination of the 8 (four 30s and four 3s) single detection magnitudes for each object in each filter were averaged together using a weighted average to calculate a magnitude and magnitude error. Notable exceptions include the i, z, and Y bands to decrease the errors: For the i-band, the 3-second exposures were matched together because they had a smaller spread in color and smaller errors than their 30-second counterparts. In the z-band, some CCDs had noticeable residual photometric offsets, even after the linear least-squares-based minimization of magnitude differences for observations of the same stars. These residual offsets were removed by applying additional offsets to align noticeably shifted stellar loci due to an individual CCD's bad calibration. The 3-second z-band exposures were averaged separately from 30-second exposures and then the two resultant averages were averaged together. For Y-band analysis, the 9 CCDs closest to the center were chosen from 2 30-second and a single 3-second exposure and weighted averages were calculated from the matches across each exposure. The remaining 30s and 3s exposure measurements were not included in the filter. In the final catalog, if a measurement is present for a given object in a given filter, there were at least two measurements of that object obtained in that filter. All matches were made to be within $0.5''$ from each other.

Positions for most objects were composed of four 30-second r-band exposures and the two 30-second i-band exposures with the best seeing. These longer r and i exposures have the best seeing and by calculating weighted averages, we can improve the positions.These are denoted in Table 3 with a capital 'A' for astrometric solution. When only the positions of photometric averages from the r-band exposures are available, they are denoted in the table with a capital 'P' for photometric. The astrometric accuracy of the 'A' objects are better in general than the positions of the 'P' objects. As a rough guide, 'A' positions are good to $\sim$ 20 mas per coordinate for stars brighter than 19th magnitude, while 'P' positions may be good to 40 mas or have systematics in them. The positions are on the reference system of the UCAC-4 reference frame.

In an excerpt of Table 3 (full table electronically available), we present a list of over 686,000 stars over a 3 square degree field of view centered on ω Cen with imaging data from 6 DECam filters. In addition to each object's position, the magnitude and a magnitude error is presented when available, along with 'N', the number of detections combined for that object in that filter. The magnitude error is weighted, and assumes that the object is constant in brightness. If the object changes significantly in brightness between detections, that will be reflected in the magnitude error, however, the error could also be due to systematics in the calibration between observations.

We also present Gaia astrometry and photometry for stars matching the DES dataset in Table 4. In addition to Gaia's coordinates and proper motions, parallax, and respective errors, we also include the G magnitude, and colors from the blue and red passbands as well as DES filters. For about two hundred stars, radial velocities were also available.

Column	Name	Description
1	RA	Right Ascension (J2000)
2	Dec	Declination (J2000)
3	N	Number of Stars to Measure Position
4	Source	Source of Position Measurement (Astrometric or Photometric)
5	u	Mean Magnitude in u
6	u_{err}	Error in u magnitude
7	N_u	Number of stars to calculate average u magnitude
8	g	Mean Magnitude in g
9	g_{err}	Error in g magnitude
10	N_g	Number of stars to calculate average g magnitude
11	r	Mean Magnitude in r
2	r_{err}	Error in r magnitude
13	N_r	Number of stars to calculate average r magnitude
14	i	Mean Magnitude in i
15	i_{err}	Error in i magnitude
16	N_i	Number of stars to calculate average i magnitude
7	z	Mean Magnitude in z
18	z_{err}	Error in z magnitude
19	N_z	Number of stars to calculate average z magnitude
20	Y	Mean Magnitude in Y
1	Y_{err}	Error in u magnitude
22	N_Y	Number of stars to calculate average Y magnitude

Table 2: Description of DECam object table

RA	Dec	N	S	u	u_{err}	N_u	g	g_{err}	N_g	r	r_{err}	N_r	i	i_{err}	N_i	z
201.686946744	-47.656090342	6	A	20.8218	0.0663	4	20.0638	0.1496	8	19.5469	0.1373	8	19.3628	0.0932	4	...
201.686955474	-47.382794931	6	A	19.3737	1.0581	5	18.892	0.0926	7	18.4007	0.0773	8	18.2349	0.0819	4	18.2632
201.686957883	-47.476388246	2	A	...	...	.	17.4399	0.0704	3	17.2358	0.3081	3	16.6687	0.3405	3	...
201.686962231	-47.516052874	5	A	18.3784	0.1212	6	17.1978	0.0796	6	16.5584	0.0921	7	16.3437	0.0194	4	...
201.686966753	-47.479080515	6	A	18.3494	0.2010	2	17.5644	0.1993	4	16.8977	0.1338	8	16.6561	0.1304	4	...
201.686968774	-47.361984941	6	A	19.8563	0.0389	3	19.1549	0.1097	7	18.6037	0.0822	7	18.399	0.0301	4	18.3822
201.686969122	-47.431661440	2	P	...	...	.	...	...	.	15.8231	0.0178	2	...	...	.	...
201.686971325	-47.351816441	6	A	20.4367	0.0451	2	19.6619	0.0523	5	19.1089	0.0211	8	18.9162	0.0561	4	18.8331
201.686971668	-47.407064703	3	A	18.6875	2.2686	3	...	...	.	18.9819	0.3980	3	19.307	0.1170	2	...
201.686972746	-47.163982462	5	A	...	...	.	...	...	.	22.7127	0.1571	3	...	...	.	22.144

Table 3: DECam ωCen and field objects

RA	Dec	μ_α	μ_α error	μ_δ	μ_δ error	π(parallax)	π
200.191874617999	-47.271504786065	-3.3314861253795	0.21047116532662	-6.3507787226319	0.28690681434841	0.21561509721248	0.15382
200.238578231489	-47.272042684839	-2.4284113629075	0.82209656776662	-7.6071049636373	1.11843836790173	0.03728020458536	0.51541
200.272071125728	-47.362025790152	-2.9820656015628	0.37370520668863	-6.8633953922860	0.50596805668067	0.08475423831059	0.26010
200.273384204089	-47.287994510015	-2.8060359509417	0.52298028289537	-6.7637491475367	0.63931754562327	-0.0761174664590	0.33138
200.293736615427	-47.469806631591	-2.9460697243861	0.58165403940112	-7.1672696991384	0.73128257964874	0.06567768109376	0.35439
200.296662614230	-47.472110930055	-2.7240585049787	0.15859433939524	-6.0985773555227	0.20428308253928	0.44429896913751	0.10325
200.315970088662	-47.462744044638	-3.9576292499979	1.06134652308362	-6.6452656100771	0.73929137031456	-0.9561207645780	0.56467
200.321740733930	-47.354572082402	-3.1459047761926	0.32620933479268	-6.7469295301745	0.29547475239966	0.19891175106293	0.21328
200.375574193081	-47.352534823086	-3.3914906581606	0.68791933576396	-6.4467700128845	0.57759908439125	-0.1122109584749	0.46449
200.384199655016	-47.611893143881	-3.7625831327275	0.45371873675897	-6.1091606626163	0.44053196545892	0.08162686139373	0.34103

Table 4: Gaia DR2 DECam matched objects

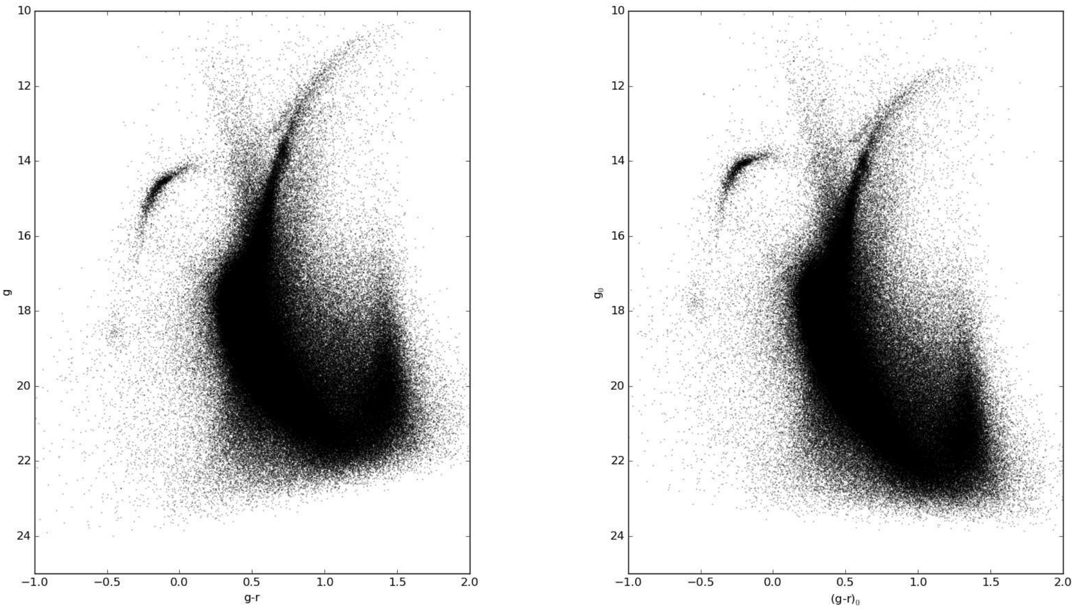

Fig. 5.— Color-magnitude diagrams for g versus g-r (left panel) and g_0 versus (g-r)$_0$ (right panel) for all the DES stars with g magnitudes (no match to Gaia DR2, therefore many field non-cluster members are present). The main sequence extends to magnitude 23 in g beyond $10'$ from the center.

6. Results

6.1. Stellar populations changing as a function of radius – the reddest sub-giant branch component

Figure 5 uses the full DES-only catalog for photometry, with 440,227 stars that have g magnitudes. The stars saturate below 9th magnitude, but extend all the way down the main sequence to 24th magnitude, as shown in the left panel. The g and r magnitudes for each star were dereddened using E(B-V) converted to DES colors, which is shown in the right panel.Many of these stars are part of the disk or halo, so we use Gaia DR2 to select stars with proper motions consistent with the cluster for further analysis in color-magnitude space.

Figure 6 shows color-magnitude diagrams for g_0 versus $(g-r)_0$ for stars at increments of $10'$ from the center of the cluster. The sub-, red-, and asymptotic-giant branches weaken as the distance from the cluster center increases. Beyond a radius of $40'$ from the center, only the main sequence is visible. The horizontal branch is barely visible beyond $30'$ from the center, and the extended horizontal branch is present at (g-r)$_0$ $\sim$0. Blue straggler stars are also visible with radii

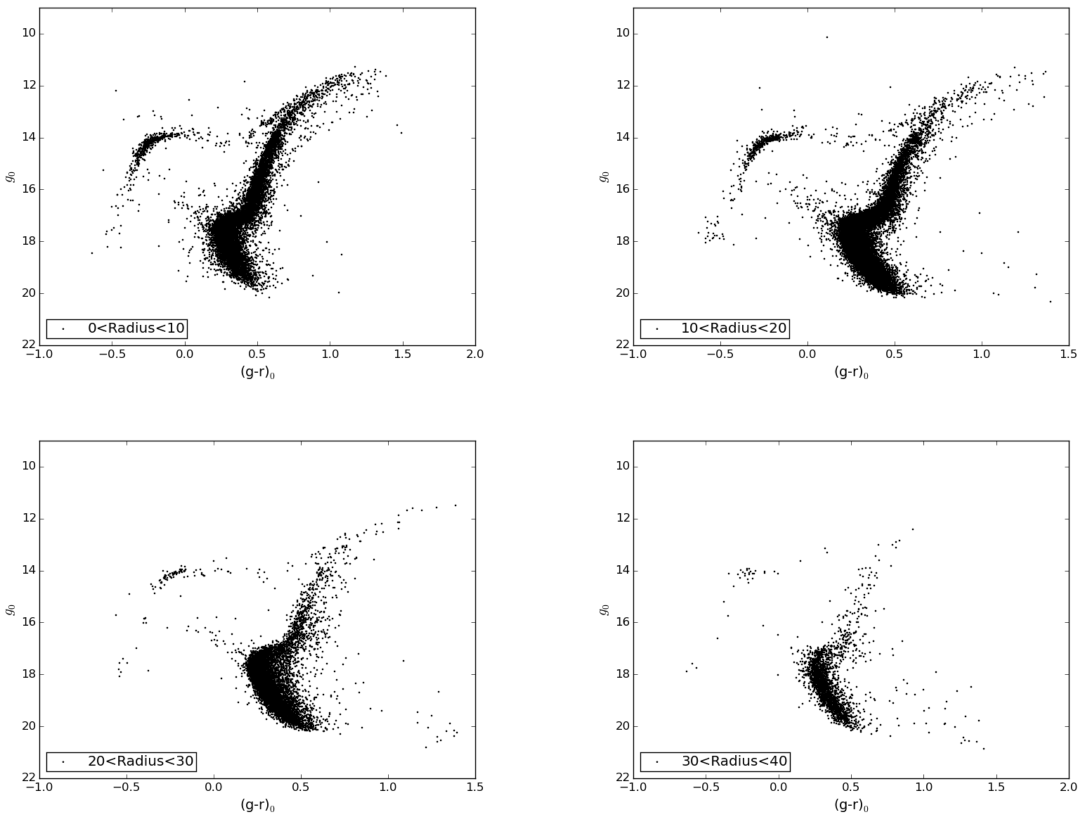

Fig. 6.— Color-magnitude diagrams for g_0 using DES and proper-motion selected Gaia matches, versus $(g-r)_0$. The sub-, red-, and asymptotic-giant branches, as well as an extended horizontal branch, weaken as the distance increases.

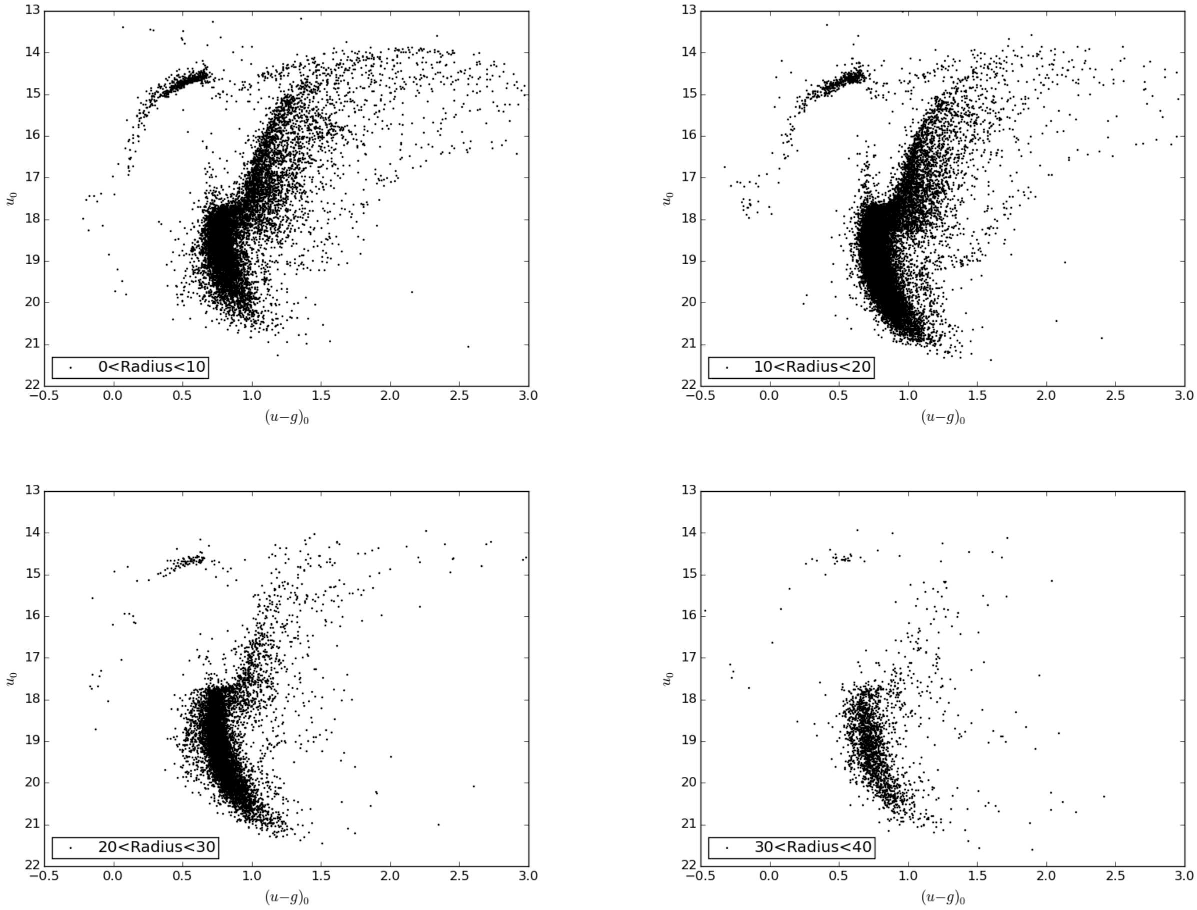

Fig. 7.— Color-magnitude diagrams for u_0 versus (u-g)$_0$ for stars at increments of $10'$ from the center of the cluster. Multiple sub- and red-giant branches weaken as the distance increases.

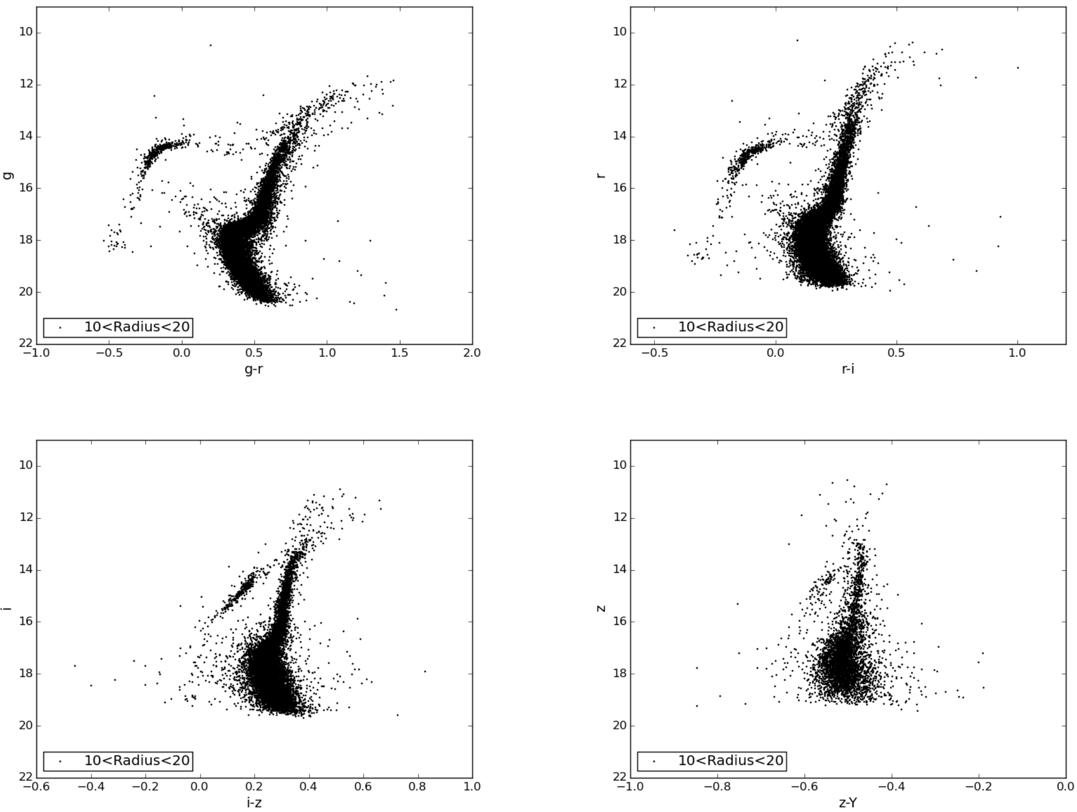

Fig. 8.— Color-magnitude diagrams for g versus g-r, r versus r-i, i versus i-z, and z versus z-Y for stars 10 to 20′ from the center of the cluster. The main sequence extends beyond 20th magnitude for all but z versus z-Y, and the sub-giant, red-giant, and horizontal branches are visible. There is an extended horizontal branch noticeable in 16< u <18 and 16< r <19.

<30′ from the center of the cluster.

Figure 7 shows color-magnitude diagrams for u_0 versus $(u-g)_0$ for stars at increments of 10′ from the center of the cluster. With the u filter, we are more sensitive to different populations, such as the lower sub- and red-giant branch at a magnitude >19, visible at radii $< 30'$. The sub-, red-, and asymptotic-giant branches weaken as the distance from the cluster center increases. Beyond a radius of 30′ from the center, only the main sequence is visible, as the horizontal branch is barely visible beyond 30′ from the center, and the extended horizontal branch is more prevalent closer to the center of the cluster. Blue straggler stars are also visible with radii $< 20'$ from the center of the cluster.

Figure 8 shows color-magnitude diagrams for u versus u-g, r versus r-i, i versus i-z, and z versus z-Y. The stars were chosen to be 10 to 20′ from the center of the cluster. Each of the figures shows the main sequence, subgiant branch, red giant branch, horizontal branch, and asymptotic giant branch for stars in the cluster. RR Lyraes are also present and have been well studied previously (i.e. Braga et al. (2018)), though we do not have the time baseline coverage within our 2 hour observing window to distinguish them here. Blue straggler stars are seen at magnitudes between 17 and 18 in g. As shown in Bellini et al. (2010) in the cluster core, multiple populations are apparent in ωCen.

The horizontal branch shows an extended feature at magnitudes $16 < u < 18$ and $u - g \sim 0$ (Figures 5 through 8. These Blue Hook stars are seen at significant radii from the cluster center, out to at least 30′. Previous studies of blue hook stars were constrained to radii less than 15′ (Whitney et al. 1998; D'Cruz et al. 2000; Bailyn et al. 1992).

We plot a $(u-i, i)$ CMD in Fig. 9 to highlight six different components of the CMD. Fig. 11 shows how these populations change with radius. Two of the CMD components (the asymptotic giant branch and the blue horizontal branch) are significantly centrally concentrated compared to the main (blue) giant branch(es) and turnoff. The other three components are not centrally concentrated to such a great extent: the lower (red) giant branch, the blue stragglers and the extended horizontal branch. This is shown more clearly in Figure 12, where the ratio of BHB/RGB and LGB(lower red giant branch)/(bluer)RGB star counts vs. radius are plotted. The BHB's are concentrated out to $r \sim 20'$ (see Bellini et al. (2009)) while the LGB stars are quite evenly distributed throughout the cluster, possibly even rising in fraction at $r > 22'$. Though the extended horizontal branch (EHB) blue hook stars are many fewer in number than BHB stars, they show a cumulative distribution in Figure 11 which is not nearly so concentrated as the BHBs in the inner 20′.

To study the relative distributions of the upper and lower giant branches in more detail, in Figure10, we compare normalized histograms of these two CMD components. In the right panel, we zoom into $10' < r < 40'$. Between 7-15′, the upper giant branch has significantly more stars than the lower giant branch, but the lower branch has more stars consistently throughout the rest of the spatial area analyzed, especially the excess between 20-40′.

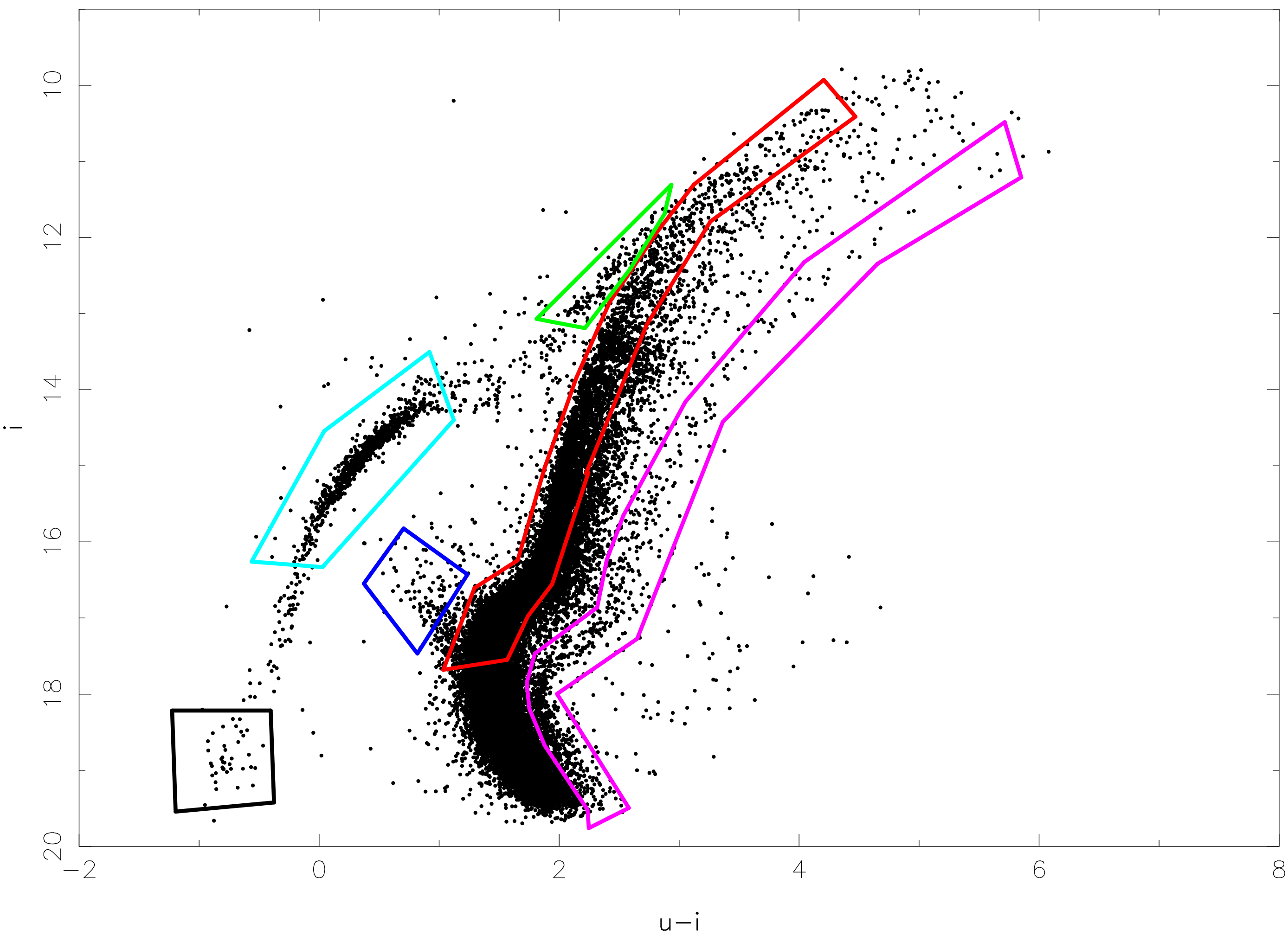

Fig. 9.— (u-i,i) CMD for stars matched to Gaia and with cluster proper motions. Six different CMD components are identified: Upper Giant Branch, Lower Giant Branch, Asymptotic Giant Branch, Blue Horizontal Branch, Blue Stragglers, and Extended Horizontal Branch.

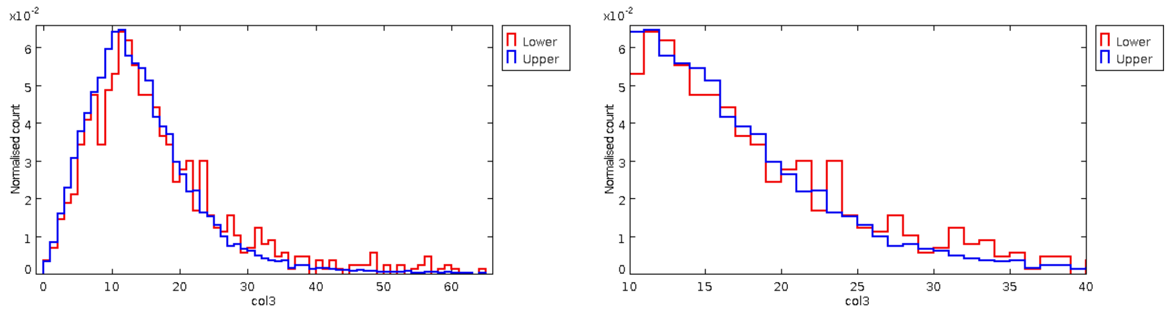

Fig. 10.— Normalized histogram of the spatial distribution of the upper and lower giant branches. The right panel zooms in between $10' < r < 40'$.

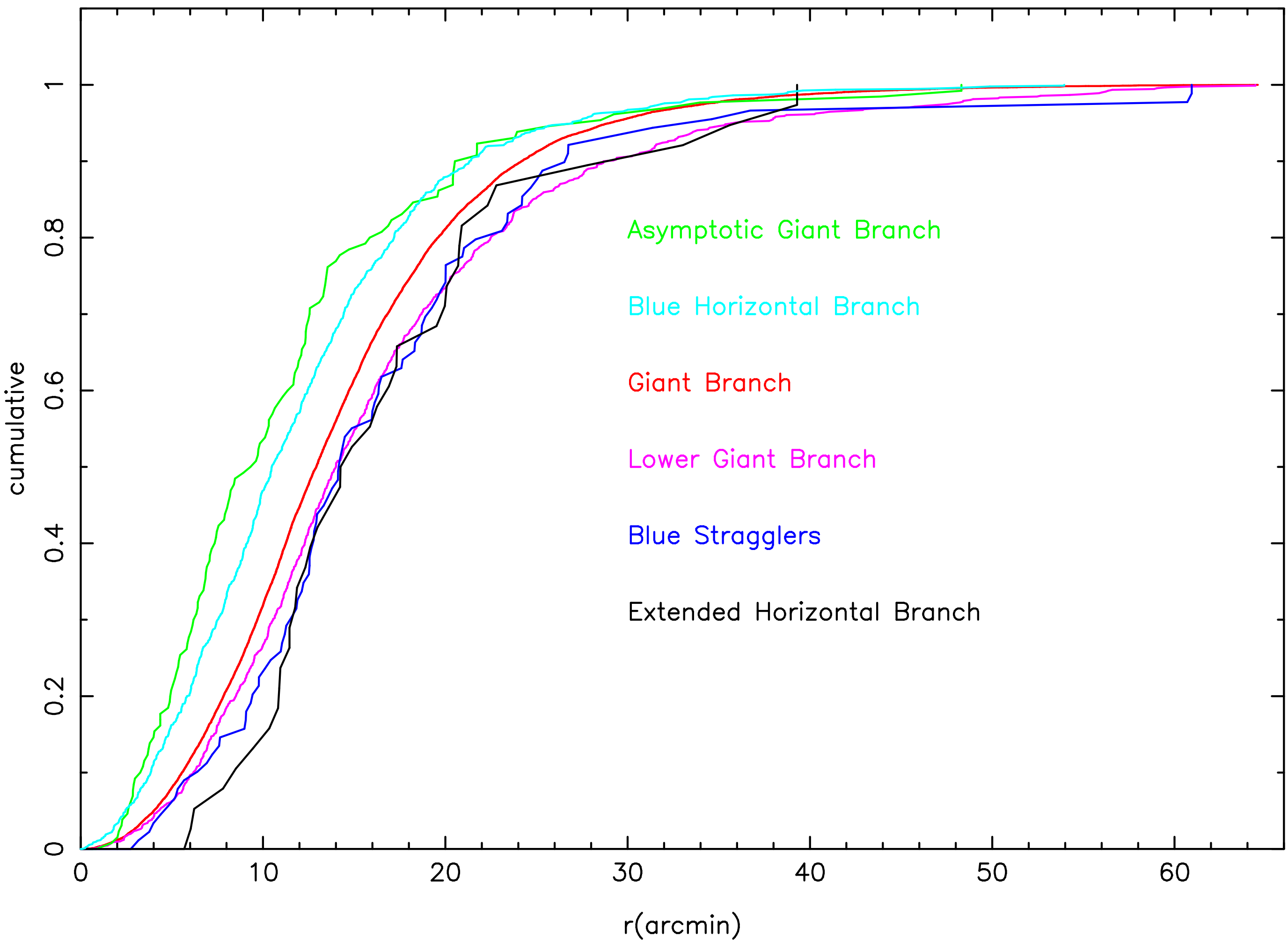

Fig. 11.— Cumulative distribution of the six populations shown in the previous figure. The AGB and BHB populations are centrally concentrated, while the LGB (lower redder giant branch), the Blue stragglers and the Extended blue hook horizontal branch stars are more radially extended in their distributions throughout the cluster.

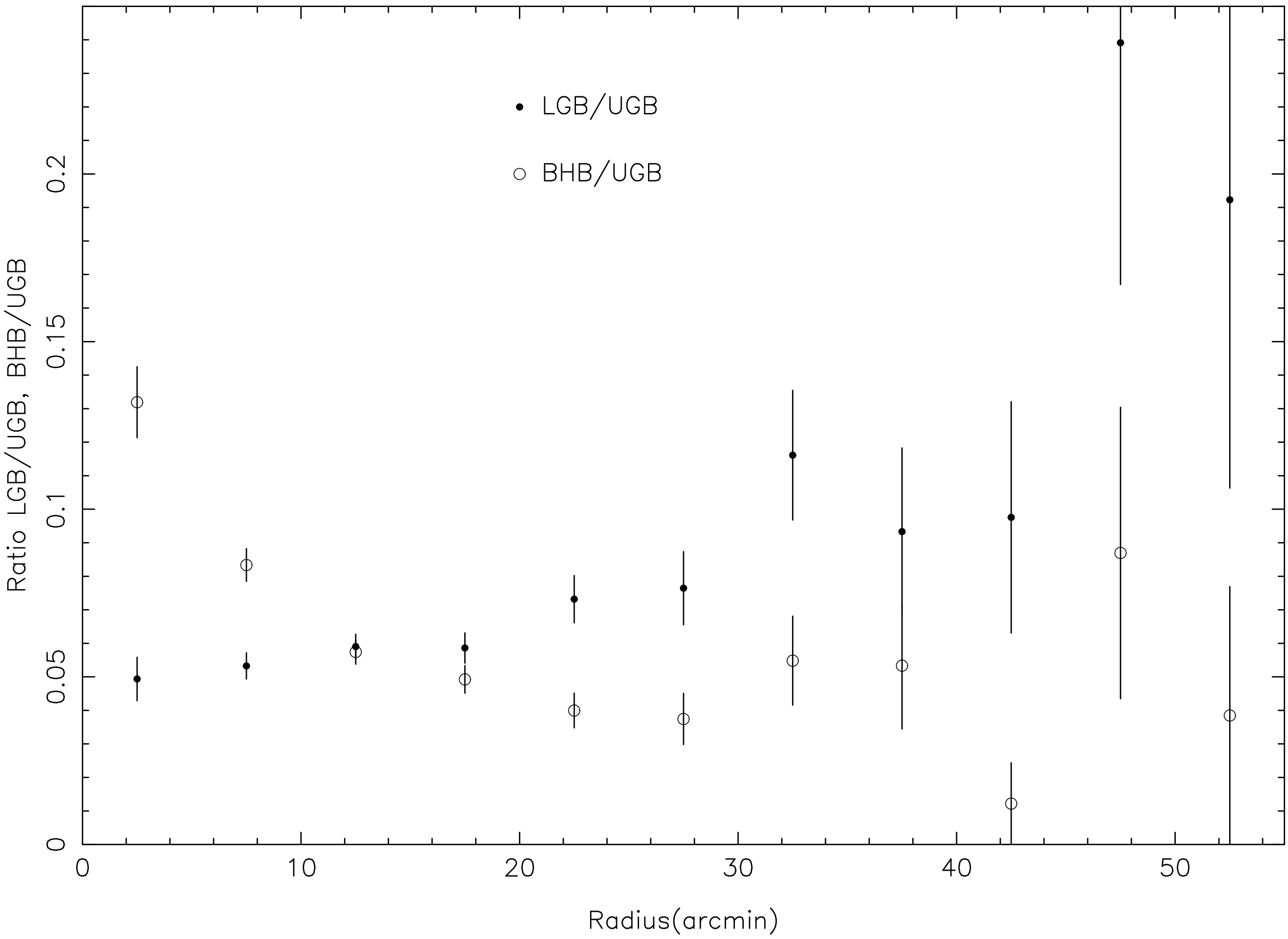

Fig. 12.— Ratio of Lower (red) giant branch to upper giant branch stars and BHB to upper giant branch stars as a function of distance from the cluster center.

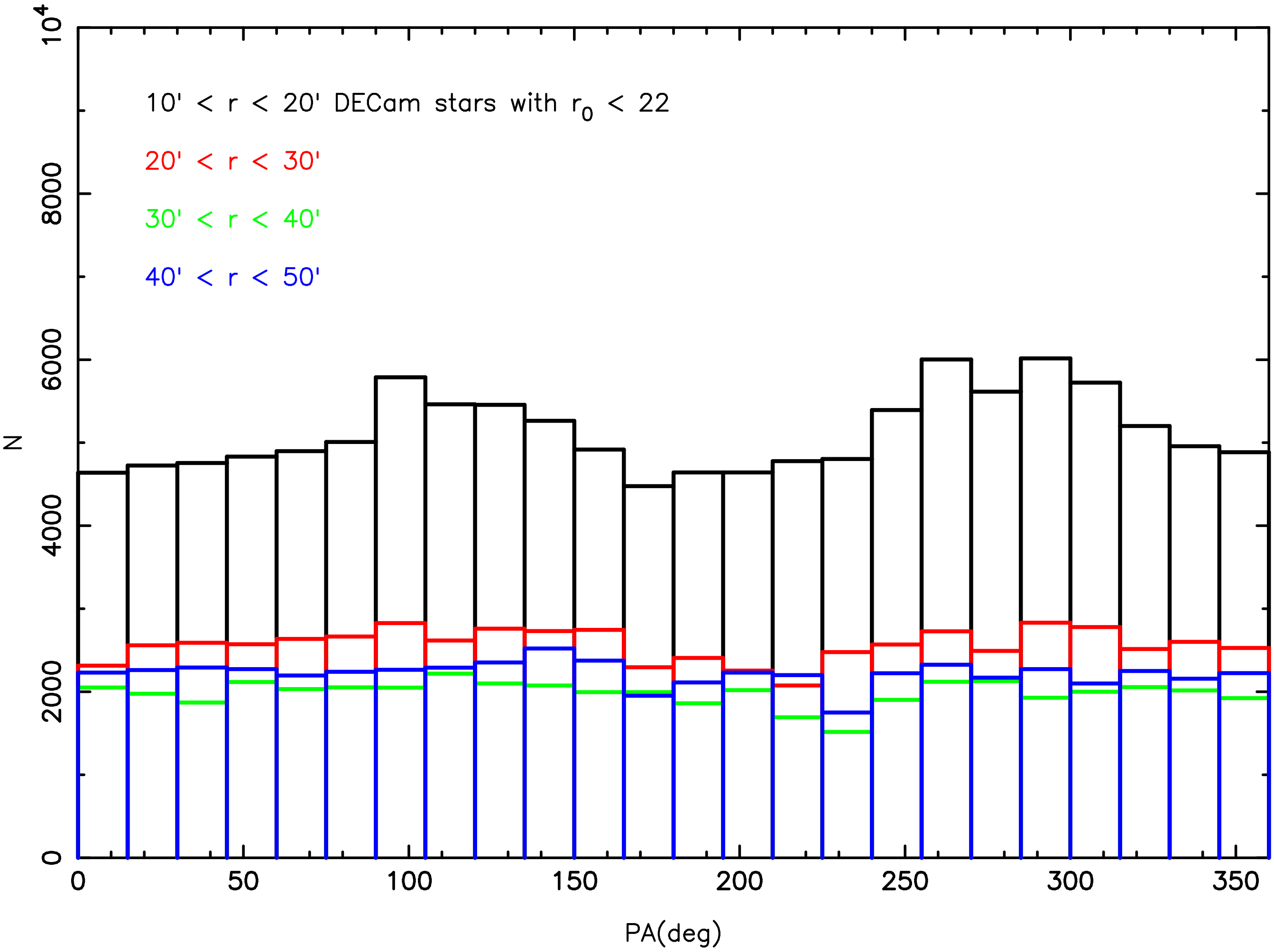

Fig. 13.— Histogram of PA of DECam star counts in 4 rings: $10 < r < 20, 20 < r < 30, 30 < r < 40, 40 < r < 50$.

6.2. Using Gaia DR2 to explore near field extra-tidal cluster members

6.2.1. Selecting the Gaia DR2 sample

While earlier searches (Majewski et al. 2012; Myeong et al. 2018) have found evidence for giant stars moving on retrograde orbits many kiloparsecs from the cluster, efforts to locate stars just beyond the tidal radius have had more mixed results (Law et al. 2003). Marconi et al. (2014) has recently again found evidence for tidal tails, though at a different P.A. than earlier searches. The accurate proper motions, parallax and G,$bp-rp$ photometry of Gaia DR2 allows a more refined opportunity to separate cluster member stars from field stars in the outer parts of the cluster in the low Galactic latitude field ($b = +15°$).

We use the Gaia DR2 ADQL interface to select 1.6 million star positions, magnitudes, proper motion, parallax, and associated errors for all objects within 3 degrees of the cluster center. Gaia DR2 radial velocities are also available for a small subset of brighter stars (mostly $G < 15$). Stars with proper motion errors per coordinate of greater than 1.5 mas yr^{-1} are excluded; this removes relatively few stars near the cluster. A new Gaia DR2 cut places stars into two groups based on proper motion: a 'field off-cluster' subset with proper motions in the box $(-8 < \mu_\alpha < -4, -4 < \mu_\delta < 0)$ mas/yr and an on-cluster subset with $(-3.9 < \mu_\alpha < -2.5, -7.3 < \mu_\delta < -5.9)$ mas/yr. Parallax information with errors are available for all stars in these subsamples. We refine the on-cluster subsample to only contain stars with $\pi < 0.2$ because Gaia DR2 has known systematics in the parallax, with parallaxes systematically underestimated by typically 0.07 (Zinn et al. 2018; Stassun & Torres 2018). We adopt a literature value of 5.16 kpc ($\pi = 0.1237 + 0.07$) for the distance from the sun to the cluster.

Further, we use the fiducial locus in color-magnitude space of cluster stars (similar to that of Figure 9 except in G, bp-rp CMD space) compared with a typical field 'locus' (with similar magnitude and color range limits sampled) and require that stars in the on-cluster sample lie within the cluster color-magnitude locus and stars in the off-cluster sample lie within the field box in color magnitude space. The on-cluster locus is wide enough to allow for color excess variations across the field of view of delta E(B-V) ~ 0.1 mag, which is similar to the color variation expected across the field. We further reduce possible reddening effects on our sampling by limiting ourselves to stars with $G < 20$, about 0.5 mags brighter than the Gaia DR2 limit in both the on-cluster and off-cluster CMD selected subsamples. This helps reduce bias from stars at the limiting magnitude from leaking in or out of the sample based on reddening alone.

6.2.2. Center of the cluster and flattening

Stars are binned in azimuth in 30° wedges in a range of annuli centered on the cluster center $(\alpha, \delta) = (201.69683, -47.47096)$. We originally attempted to use the most recent cluster center position given by Helmi et al. (2018), but found it to give lopsided, one-hump azimuthal plots (see

Fig. 13) suggestive of a mis-centering. The Helmi et al. (2018) cluster center appears to have been affected by Gaia DR2 incompleteness in the central parts – resulting in a miscentering by about 3.3′W, 0.3′S from what appears to be a more accurate center given by Harris (2010). Figure 13 shows star counts for the on-cluster subsample as a function of azimuth (P.A. N through E). As has been previously noted, the central portions of the cluster are slightly flattened. We find a P.A. of about 0-10 degrees in the inner 20′ and slightly higher P.A. and much less significant flattening as one goes out. We return to this below when discussing differential cluster rotation.

6.2.3. Asymmetrical distribution of outer cluster member stars

Figure 14 shows the distribution of on-cluster candidate members in red and field stars matching the off-cluster cuts in black. Stars closer than 18′ to the cluster center are not included. The green segment shows the rotation axis of the cluster from HST analysis of Anderson & van der Marel (2009). The long red arrow shows the projected direction of cluster motion through space in the from Gaia (and consistent HST) proper motion data, corrected for the solor reflex motion.

As shown in Figure 2, the Gaia DR2 catalog is not 100% complete. Therefore a more accurate estimate of cluster stars at large radii is obtained by taking the ratio of on-cluster to off-cluster counts in each 30° wedge. Figure 15 shows these ratios of members to field stars vs. P.A. At many radii, there are extra cluster member stars at these characteristic azimuths.

Presenting the information from Fig. 15 schematically and counting stars in each 30 degree azimuthal wedge for a variety of radial annuli, we show in Fig. 16 the wedges from Fig. 14 which have signifcant ($> 3\sigma$) excesses in on-cluster star counts over the background. Figure 16 shows the same range of radii from 36′ to 120′. This shows that at radii $\sim 50'$ there is an excess of cluster candidates at azimuths of P.A. $165°, 250°$.

It is interesting to note that the excess stars at P.A. $\sim$ 105° are nearly aligned with the equatorial flattening (perpendicular to the axis of rotation) of the cluster as observed from HST observations of the cluster core. This suggests some extra-tidal stars could be preferentially escaping from the rotating cluster's equatorial belt.

6.2.4. Other overdensities

The direction of the Galactic center is toward P.A. = 95 degrees and the direction to the Galactic plane is about P.A. = 170 degrees. The excess stars at P.A. 165 degrees be part of a leading tidal stream but there seems to be no corresponding trailing stream excess at P.A. of 345 degrees. And what about the asymmetric excesses inside the $r = 72'$ tidal radius at P.A. 210 to 270 deg? Here there are 64 stars in significant excess over other azimuths at the same radii. What force(s), rotational or tidal could produce this persistent imbalance? The orbit of the cluster takes it as close as 1.5 kpc from the Galactic center (Majewski et al. 2012) (the cluster's orbit will now be slightly different from Majewski et al. (2012) based on updated Gaia DR2 and HST proper motion). The current data, with these cuts, suggest that beyond about 1.4 degrees (84 arcmin) all remaining red dots are consistent with being part of a background population (which happen to have colors and magnitudes matching the cluster), given the small number statistics. We use the number of red dots at 2 to 3 degrees from the cluster to serve as a background as there's no significant variation vs. azimuth at these radii and then can estimate the number of cluster stars at each radii from about 0.8 degrees to 1.4 degrees. There are only ~ 9 stars at $72 < r < 180'$ which we can confidently ($> 3\sigma$ significance), say are cluster members, and all of these have $90^\circ <$ P.A. $< 120^\circ$. Both internal cluster rotation and external Galactic tidal forces could be responsible for placing some stars into asymmetric distributions beyond $r \sim 48'$. The multiple populations also suggest the cluster may have undergone merger activity in the past or had a complex and long lived star formation history.

6.2.5. Cluster Rotation

Figure 13 shows the density of stars vs. P.A. azimuth at a variety of annuli from the inner to the outer parts of the cluster. The inner most annulus plotted ($10' < r < 20'$) shows the characteristic double-peaked flattening signature, with the two peaks approximately 180° apart. The P.A. of the bulges in density correspond closely to P.A. of the rotation axis (plus 90°) as seen in Anderson & van der Marel (2009); Bianchini et al. (2018). Further out this flattening shifts to slightly higher P.A. and becomes is harder to discern. It vanishes for $r > 50'$. The cluster has a velocity dispersion of 17.6 km/s and an escape speed of about 62 km/s (from Baumgardt & Hilker (2018)). The rotation speed at radius $= 5'$ is about 6 km/s (Bianchini et al. 2018).

We examine the Gaia DR2 proper motions of cluster member to independently study the cluster's rotation. Figure 17 shows binned proper motion vectors, averaged over 30°, $10'$ wedges for candidate cluster stars (with the systemic cluster proper motion of $(-3.19, -6.74)$mas/yr) subtracted off). This shows quite strong rotation in the inner $r < 20'$, and some trends outside this radius suggestive of differential rotation or a tilting rotation axis,though much less strongly defined. The green arrow indicates the previous determination of the cluster's rotation axis.

While there are many possible configurations that can lead to the arrow pattern in Figure 17, we show in Figure 18 a simple model for inclination, differential rotation and shifting position angle which reproduces approximately the central and west portions of the cluster. The model parameters are: For $r < 30'$ $v_{rot} = 0.2$mas/yr, P.A. $= 0^\circ$; for $30 < r < 48', v_{rot} = 0.5$mas/yr, P.A. $= 20$ for $48' < r < 60'$ $v_{rot} = 0.4$mas/yr, P.A. $= 40^\circ$. Inclination is fixed at 40° (Rotation axis tipped toward the Sun by this angle) as derived in Libralato et al. (2018). The agreement near the center of the cluster and to the west is reasonable, but not so good to the East and South. A more complex model is likely required for a better fit, and can provide more clues as to the detailed kinematics and possibly evolutionary history of this cluster.

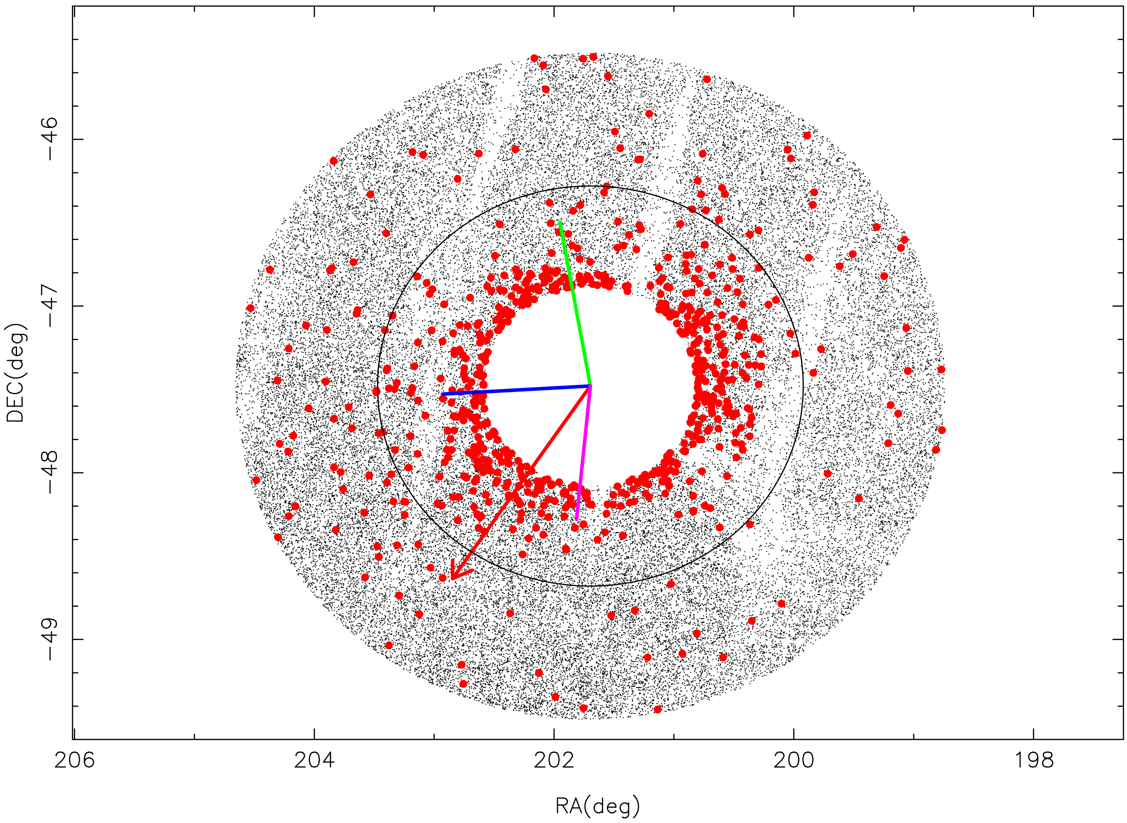

Fig. 14.— Stars with proper motion, colors and magnitudes and parallax < 0.2 mas (uncorrected) consistent with being ωCen (red dots) cluster members. There is a small but significant excess of red dots beyond the tidal radius (black circle at $72'$) at P.A. $90° - 120°$. There is also, within the tidal radius, significant excesses in cluster members at P.A.s to the SE and W. Non-cluster field stars are shown as black dots. Note the non-uniform coverage of the field, and the increased density of background stars to the southeast due to lower Galactic latitude. The green line segment is aligned with the rotation axis of the cluster. The blue line segment points toward the Galactic Center while the magenta segment points toward the Galactic plane (same Galactic longitude, but toward $b = 0°$). The long red arrow points in the direction of motion of the cluster, as determined by the cluster's proper motion.

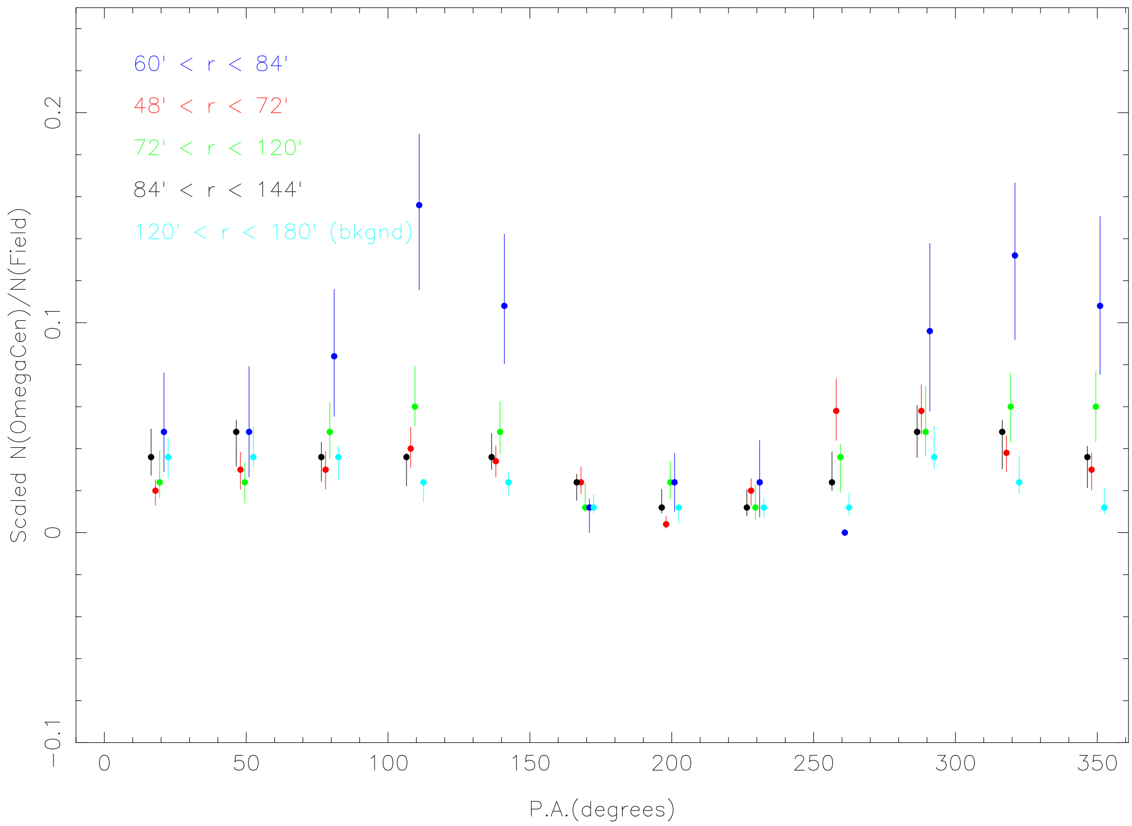

Fig. 15.— Ratios of star normalized star counts vs P.A. for several radial annular bins. Data far from the cluster ($120' < r < 180'$) are considered background with no significant excess in cluster stars present at any preferred P.A. No significant azimuthal variation is seen at these distant radii.

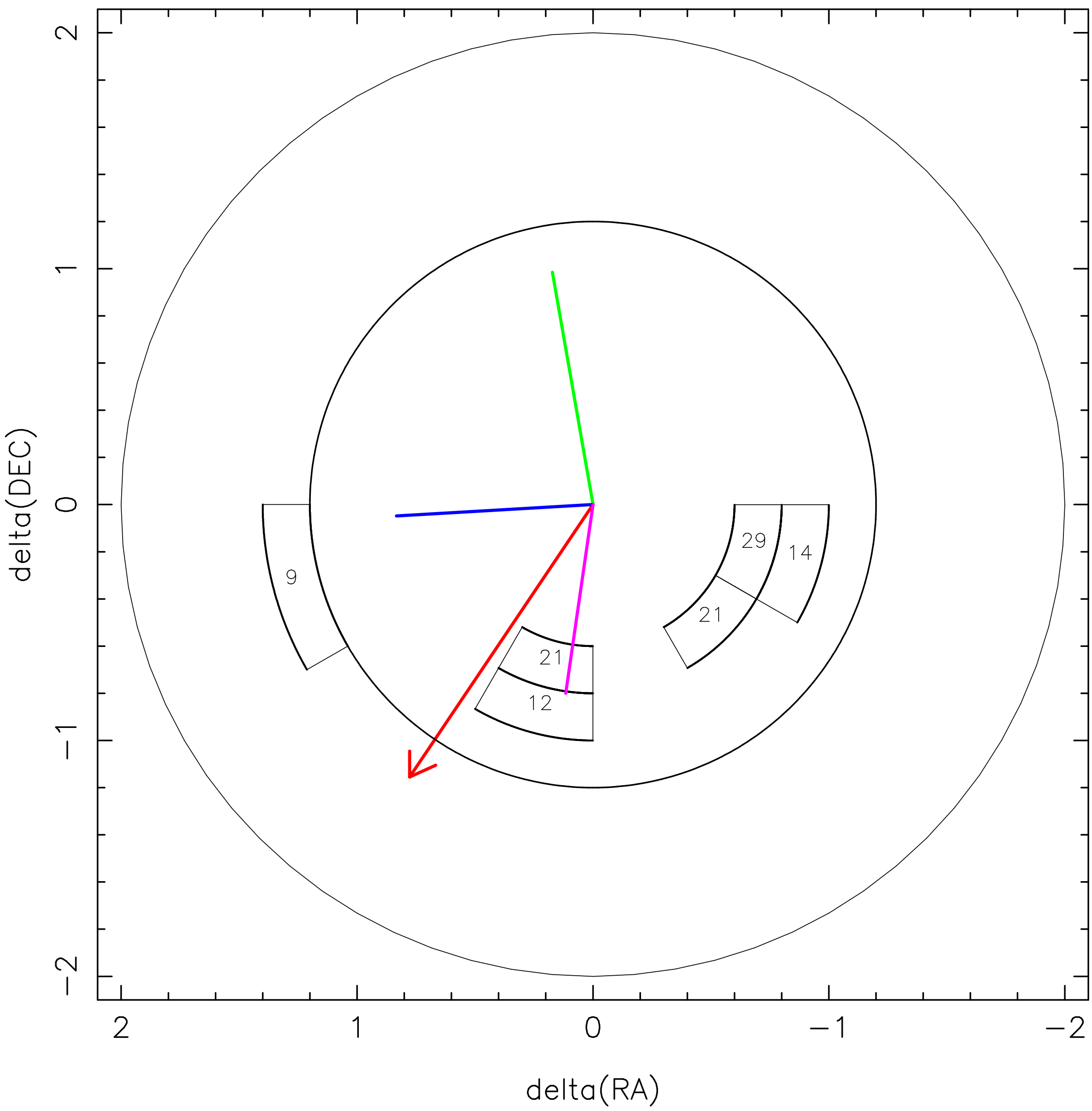

Fig. 16.— Excess cluster candidate star counts vs azimuth and radius. These are counts of the red dots in the previous figure, corrected for background contamination. Only cells with counts at $>= 3\sigma$ significance are shown. Lines indicated motion, GC, projected plane and rotation flattened major axis are as in the previous figure. This indicates 9 extra tidal stars at P.A. between $90° - 120°$ and preferred P.A. for 77 stars within the tidal radius ($36' < r < 60'$) toward P.A.s $150° - 180°$ and $210° - 270°$.

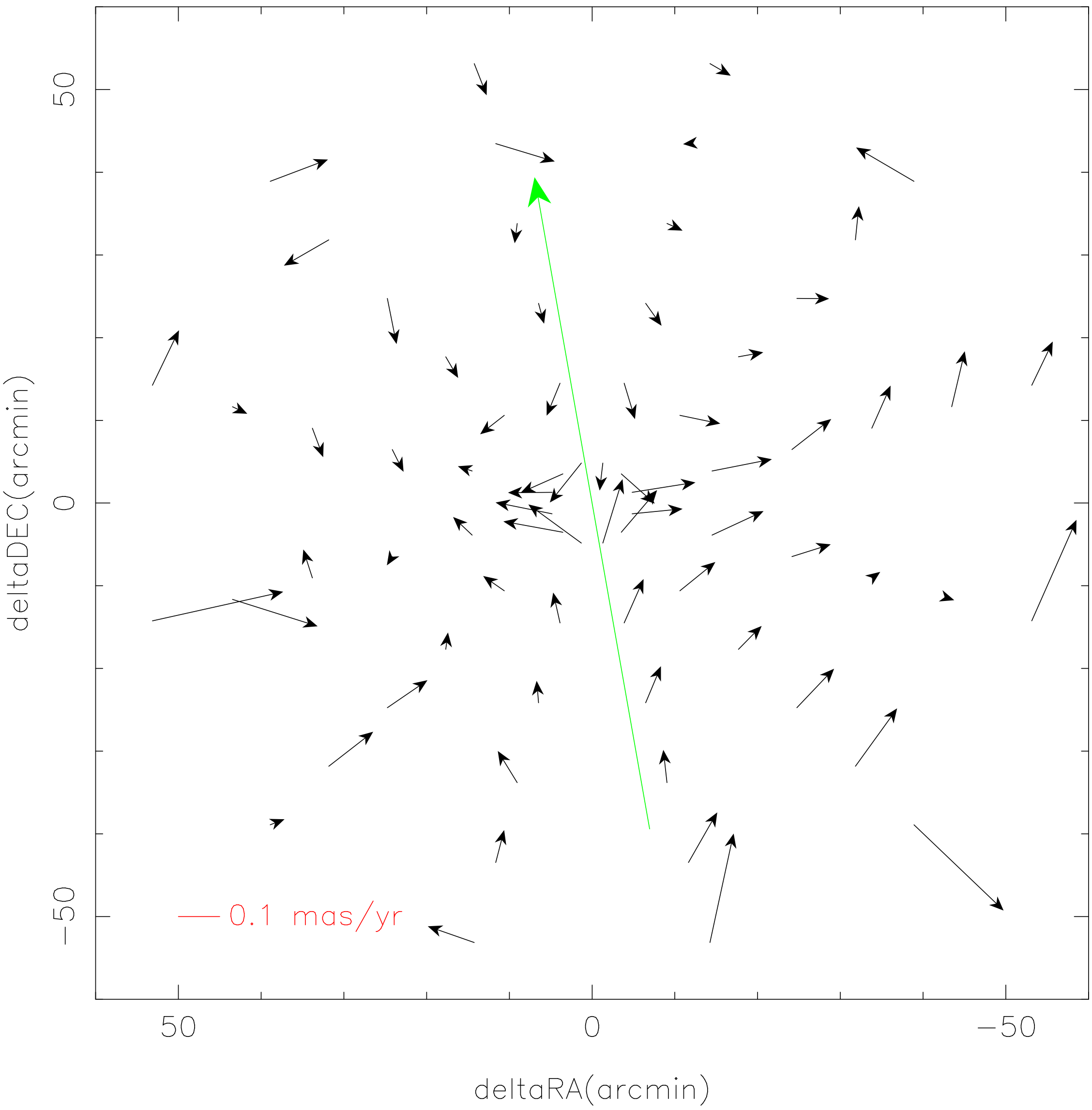

Fig. 17.— Average proper motion (with cluster pm subtracted)

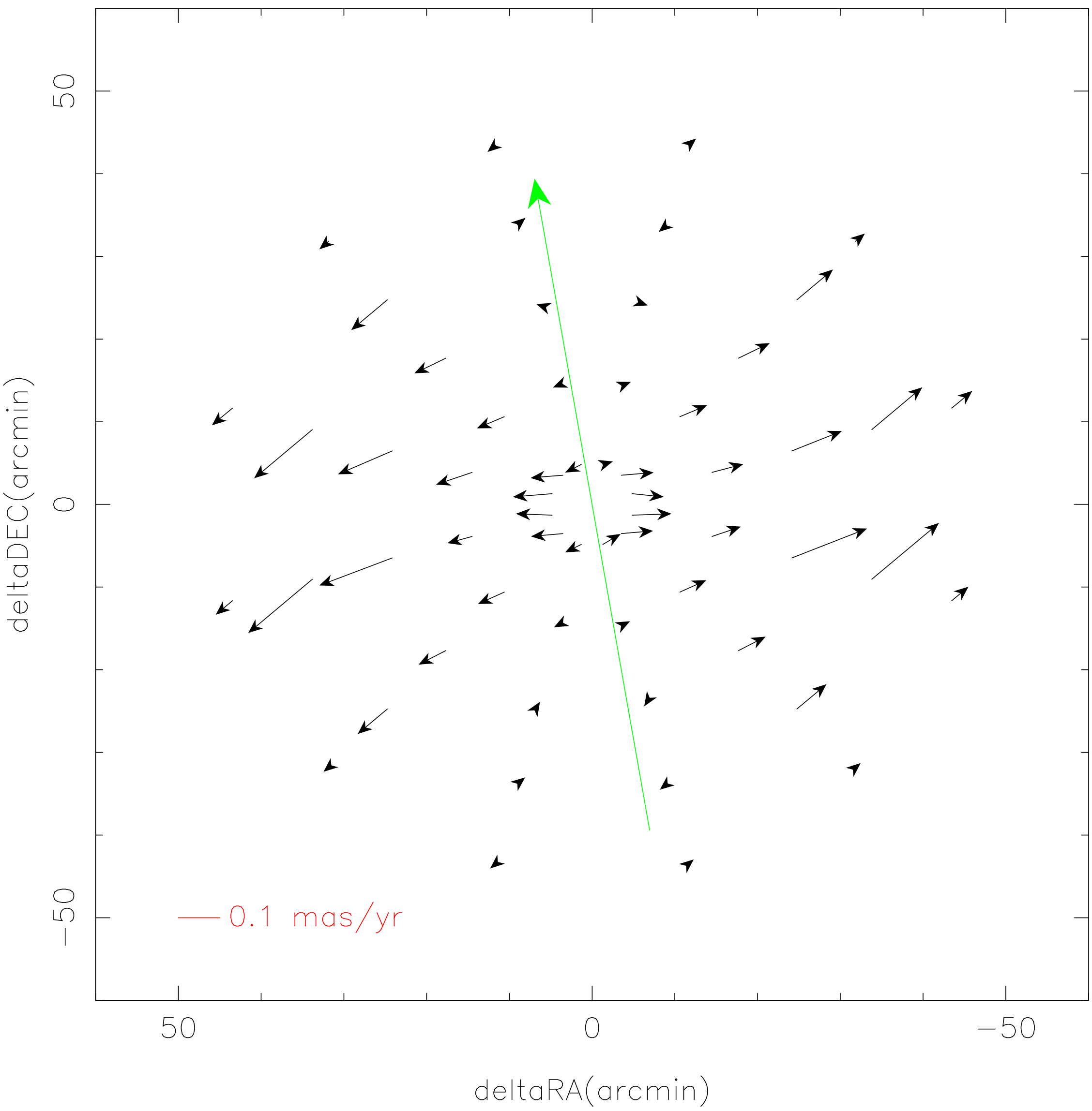

Fig. 18.— Model of differential angle twisting rotation of the cluster

We have attempted to determine proper motion trends for different sub-groups of stars in the cluster CMD, but other than the upper giant branch, which mimics the total proper motion of the cluster shown in Figure 17, other groups of stars (such as Blue Horizontal Branch, Blue Stragglers, etc) are too noisy to show significant trends in proper motion or rotation within the cluster.

7. Summary and Conclusions

The tables of stars presented here provides an important reference for cluster researchers who wish to use the DES DECam filter system for their work. This work provides a useful catalog of accurate multi-color photometry (including the important u-band filter) in a well known cluster valuable for stellar population work.

7.1. Stellar population distributions in ωCen

An advantage to understanding globular clusters is that their characteristics are a key to understanding galaxies. Photometric information, such as color-magnitude diagrams as a snapshot into the formation and evolution of the cluster, provides us one way to identify stars belonging to the cluster. Prior to Gaia DR2, cluster members in the outskirts of the cluster ($r > 40'$ were not easily separated from field stars. By using a proper motion analysis, membership for stars at larger radii from the cluster center can be determined reliably. Combining the DES catalog with Gaia yields better separation of field and cluster stars based on properties of the cluster. We select on proper motion, parallax, and proximity to the stellar locus on the color-magnitude diagrams. The deep, accurate, wide-field multi-color DECam imaging of ωCen provides new insight into the distribution of the many of stellar types present in the cluster, including clear evidence of the central concentration of the AGB population. The distinct lower RGB and BS populations are *not* centrally concentrated, but rather extend out to the tidal radius. This is consistent with the work of Calamida et al. (2017) that the reddest sub-giant and giant branch is more radially extended than the brighter and bluer (main) giant branch. Most previous photometric studies were confined to radial distances $r < 30'$, but using Gaia DR2 proper motions as a discrimiator, the accurate DES photometry becomes useful to $r \sim 50'$ and beyond. We also find that the BHBs are more centrally concentrated than the EHB (blue hook) stars, though the fainter EHBs are no longer visible in color-magnitude diagrams with stars that have radii greater than $40'$.

7.2. Near field distribution of extra-tidal and near tidal cluster members

As we can trace populations out to the tidal radius and beyond, we look for extra-tidal excesses. Given the finding of Dinescu et al. (1999) that the cluster takes approximately 120 Myr to circumnavigate the galaxy in a retrograde manner, van de Ven et al. (2006) estimated that the cluster spends approximately 10% of the orbit around the galaxy within the plane of the disc. Da Costa & Coleman (2008) extrapolated that the average velocity change per pass through the plane is approximately 0.17r, where r is the radial distance from the center in arcminutes. The tidal shocks could give the loosely bound outer cluster stars enough velocity to escape. Stars traveling 1 km/s would be 1-2 tidal radii away from the cluster within an orbital period. The dispersing cluster Pal 5's become noticeable at about twice the tidal radii Odenkirchen et al. (2003) and so it makes sense to search that far away from ωCen for similar tails.

With the release of Gaia DR2, we searched 3 degrees from the center of the cluster and find very few cluster candidates outside of the tidal radius. Only 9 stars at $72' < r < 84'$, at a P.A. of 105°, in fact, in a cluster of more than one million stars. This is consistent with most previous near field searches.

While we don't see extra-tidal tails, we do see the excess of stars at non-symmetric position angles (less than 180° from each other). While some of the excess could be caused by the flattening of the rotating cluster, resulting in the ejection of stars, other asymmetries points more towards the nearby Galactic plane. Finally, there is a significant excess of 64 tidal stars at $48' < r < 72'$, with azimuth 210<PA< 270°, somewhat in the direction away from the Galactic Center, but not convincingly enough to suggest a strong tidal effect. We would expect an overdensity of stars affected by the Galactic potential to have 'trailing tail' P.A.s near 330°, but these are not seen.

Gaia DR2 proper motions give new insight into the rotation structure of the cluster, and we find further evidence beyond Libralato et al. (2018) of differential rotation and possible evidence for a rotation axis which changes as a function of radius from the cluster center.

Combining precise multi-color DES photometry with Gaia DR2 proper motions offer a few more insights into the remarkable cluster ωCentauri, even as it remains unique in its layered complexity.

REFERENCES

Abbott, T, et al. https://arxiv.org/abs/1801.03181

Anderson, J., & van der Marel, R. P. 2010, ApJ, 710, 1032

Antilogus, P., Astier, P., Doherty, P., Guyonnet, A., & Regnault, N. 2014, Journal of Instrumentation, 9, C03048

Bailyn, C. D., Sarajedini, A., Cohn, H., Lugger, P. M., & Grindlay, J. E. 1992, AJ, 103, 1564

Baumgardt, H., & Hilker, M. 2018, MNRAS,

Bekki, K. & Freeman, K. C. 2003, MNRAS, 346, L11

Bellini, A., Piotto, G., Bedin, L. R., et al. 2009, A&A, 493, 959

Bellini, A., Bedin, L.R., Piotto, G., Milone, A.P., Marino, A.F., & Villanova, S. 2010 AJ, 140, 631

Bertin, E., & Arnouts, S. 1996, A&AS, 117, 393

Bertin, E. 2006, Astronomical Data Analysis Software and Systems XV, 351, 112

Bianchini, P., van der Marel, R. P., del Pino, A., et al. 2018, arXiv:1806.02580

Braga, V. F., Stetson, P. B., Bono, G. et al. 2018 AJ 155, 137

Brown, T. M., Sweigart, A. V., Lanz, T., Landsman, W. B., & Hubeny, I. 2001, ApJ, 562, 368

Burke, D. L., Rykoff, E. S., Allam, S., et al. 2018 AJ 155, 41.

Calamida, A., Bono, G., Stetson, P., et al. 2009 ApJ 706, 1277

Calamida, A., Strampelli, G., Rest, A. et al. 2017 AJ, 153, 175

D'Cruz, N. L., O'Connell, R. W., Rood, R. T., et al. 2000, ApJ, 530, 352

Da Costa, G. S., & Coleman, M. G. 2008, AJ, 136, 506

Dehnen, W. & Binney, J. J. 1998 MNRAS 298, 387

Dinescu, D. I., Girard, T. M., & van Altena, W. F. 1999, AJ, 117, 1792

Flaugher, B. et al. 2015, AJ 150, 150

Frieman, J. & DES Collaboration, 2005, arXiv:astro-ph/0501346

Frieman, J. & DES Collaboration, 2013, AAS Abstracts 221, 335.01

Fernández-Trincado, J. G., Vivas, A. K., Mateu, C. E., et al. 2014, arXiv:1411.3004

Gaia Collaboration arXiv:1804.09365

Harris, W. E. 1996, AJ, 112, 1487

Harris, W. E. 2010, arXiv:1012.3224

Gaia Collaboration, Helmi, A. et al. 2018 åsubmitted arXiv:1804.09381

Honscheid, K., DePoy, D. L., & for the DES Collaboration 2008, arXiv:0810.3600

Johnson, D. R. H. & Soderblom, D. R. 1987 AJ 93, 864

Law, D. R., Majewski, S. R., Skrutskie, M. F., Carpenter, J. M., & Ayub, H. F. 2003, AJ, 126, 1871

Lee, J.-W., Kang, Y.-W.,Lee, J., & Lee, Y.-W. 2009, Nature, 462, 480

Leon, S., Meylan, G., & Combes, F. 2000, A&A, 359, 907

Libralato, M., Bellini, A., Bedin, L. R., et al. 2018 ApJ, 854, L45

Majewski, S. R., Nidever, D. L., Smith, V. V., Damke, G. J., Kunkel, W. E., Patterson, R. J., Bizyaev, D., Garcia Perez, A. E. 2012, ApJ, 747, LL37

Marconi, M., Musella, I., Di Criscienzo, M., et al. 2014, MNRAS, 444, 3809

McWilliam, A., & Smecker-Hane, T. A. 2005, ApJ, 622, L29

Morganson, E. et al. 2018, PASP 130, 4501

Myeong, G. C., Evans, N. W., Belokurov, V., Sanders, J. L., & Koposov, S. 2018 arXiv:1804.07050

Odenkirchen, M., Grebel, E. K., Dehnen, W., et al. 2003, AJ, 126, 2385

Piotto, G., Villanova, S., Bedin, L. R., et al. 2005, ApJ, 621, 777

Plazas, A. A., Bernstein, G. M., & Sheldon, E. S. 2014, Journal of Instrumentation, 9, C04001

Roeser, S., Demleitner, M., & Schilbach, E. 2010, AJ, 139, 2440

Stassun, K. G. & Torres, G. 2018 arXiv:1805.03526

White, R. & Shawl S. J. 1987 ApJ317, 246

Whitney, J. H., Rood, R. T., O'Connell, R. W., et al. 1998, ApJ, 495, 284

van de Ven, G., van den Bosch, R. C. E., Verolme, E. K., & de Zeeuw, P. T. 2006, A&A, 445, 513

van Leeuwen, F., Le Poole, R. S., Reijns, R. A., Freeman, K. C., & de Zeeuw, P. T. 2000, A&A, 360, 472

van Leeuwen, F. & Le Poole, R. S. 2002 PASP conf. Series. 265 41

van Loon, J. T., van Leeuwen, F., Smalley, B., et al. 2007, MNRAS, 382, 1353

Zacharias, N., Finch, C. T., Girard, T. M., et al. 2013, AJ, 145, 44

Zinn, J. C., Pinsonneault, M. H., Huber, D, & Stello, D. 2018 arXiv:1805.02650